Politecnico
di Torino

POLITECNICO DI TORINO

Master's degree course in Aerospace Engineering
Academic year 2022/2023
Graduation Session April

Variable Swarm Strategy for small spacecraft

Supervisors:
Prof. Elisa Capello
Prof. Dario Ruggiero

Defended By:
Davide Longo

"We are not going in circles, we are going upwards.
The path is a spiral; we have already climbed many steps."

-HERMANN HESSE, SIDDHARTHA

Abstract

Recently, the concept of controlling a large group of spacecraft has been studied extensively in literature for different applications. Swarms of microsatellites are an attractive alternative to traditional large spacecraft due to the resulting enhancement in robustness of the overall mission architecture while reducing the cost of each platform. The Guidance, Navigation & Control (GNC) subsystem of the space system is required to drive and keep the satellites formation towards multiple different configurations, which are imposed by the mission objectives. It is relevant to investigate low computational effort algorithms enabling spacecrafts to achieve and keep a formation by ensuring obstacle avoidance.

The Artificial Potential Field (APF) method provides simple and effective collision-free path planning for practical terrestrial robotics control. This thesis objective is the design of an APF based method to guarantee the creation of a spacecrafts swarm formation, where each spacecraft is equidistant from each other.

The performance of the proposed method are evaluated combining the APF with a Proportional Derivative (PD) controller, and by means of extensive simulations. Each spacecraft, starting from a random initial position, moves to achieve the formation centered in the desired position. These simulations were conducted both considering the spacecrafts as the only entities in orbit and also considering both fixed and moving obstacles. The capability of the swarm to rearrange the formation according to spacecrafts number is also analyzed. In this case, once the formation has been created, one of the spacecrafts is considered inoperative and the remaining ones should rearrange themselves in a different configuration whose mean position is driven to the desired one. Finally, a proximity operation scenario was considered to evaluate the maximum dimension of the obstacle that the swarm of spacecrafts is able to avoid during the formation acquisition maneuver.

The results verify the effectiveness of the algorithm to guide the spacecrafts towards the desired configuration while avoiding obstacles using minimum computational effort.

Contents

List of Figures

List of Tables

Chapter 1

Introduction

The objective of this chapter is to provide the reader with a general overview of spacecraft formation flying and its increasing relevance in the space field. Subsequently, the motivations and contributions for this thesis work are presented.

1.1 Spacecraft Formation Flying

The definition of spacecraft formation flying is not very accurate or globally accepted. However, most of the space community agrees upon the definition proposed by NASA's Goddard Space Flight Center (GSFC): *The tracking or maintenance of a desired relative separation, orientation or position between or among spacecraft*. Therefore, spacecraft formation flying are a particular case of a more wide category, named distributed space systems, defined by NASA GSFC as follows: *An end-to-end system including two or more space vehicles and a cooperative infrastructure for science measurement, data acquisition, processing, analysis and distribution* [2]. Spacecraft formation flying can be developed following distinct approaches, that differ from each other by the kind of relationship existing among the various spacecrafts that constitute the formation.

1.1.1 Orbit tracking

Considering single satellite missions, they are commonly designed to remain in a specific orbit. However, due to the orbital perturbations, some station-keeping maneuvers are periodically performed. Therefore, this approach can be extended to formations in which each satellite is supposed to occupy a fixed desired orbit. This is a basic concept since each spacecraft is controlled separately and there is no real cooperation among them.

1.1.2 Leader/Follower

In the leader/follower approach two categories of spacecrafts can be identified: a leader spacecraft is controlled to a specific orbit and the follower spacecraft in the formation control their relative position and attitude with respect to the leader. This method has the advantage to permit most spacecrafts in the formation to follow the orbital dynamics of the leader, as a consequence only a periodic control on the relatives states of the formation have to be performed. However, since the leader spacecraft is by definition at its correct

state, the main disadvantage is that the amount of fuel required by the leader is not as much as the one required by the followers. To fix this issue and equalize the fuel consumption a possible solution is to regularly interchanging the roles of leader and followers.

1.1.3 Virtual structure

The virtual structure approach treats the whole formation as a single structure. It allows to minimize the overall state error of the formation. The main advantage with respect to the leader/follower approach is that the state error will concern all the spacecrafts in the formation. In addition, it is possible to balance the fuel consumption among the spacecrafts in the formation. The realization of such an approach involves coordinated inter-spacecraft communication.

1.1.4 Swarming

In the swarming approach the number of spacecrafts is usually greater and there is not a specific spacecraft playing a leading role. These methods have the advantage that they easily scale increasing the number of spacecrafts without arousing large communication or computation burdens. Recently, several researchers have proposed different control laws to arrange a large group of spacecrafts into a regular formation based on local information. However, these approaches are generally not optimized in terms of fuel consumption and typically do not contemplate collision avoidance.

1.2 Motivations and contributions

From the start of the manned space program, concepts for spacecraft formation flying have been investigated. At that time, the challenge was to have two spacecraft performing a rendez-vous maneuver and dock together. During the Apollo space program, when the final lunar spacecraft was assembled in orbit, this was extremely important. During this maneuver, orbit corrections are made to control and change the relative orbits of two spacecraft rather than the Earth's orbit itself. The relative distance is slowly and carefully reduced to zero for the docking procedure.

The current emphasis of spacecraft formation flying has now expanded to include the formation keeping of many spacecraft. For example, the U.S. Air Force is investigating the possibility of forming a sparse aperture radar dish in space using a cluster of similar spacecraft. The use of many satellites flying at a fixed geometry avoids the considerable technological and cost challenges of attempting to build an equivalent-sized radar dish. The sizes of these satellite structures can range from a few tens of meters to several kilometers. Attempting to build, control, and navigate a lightweight radar dish structure that could span several kilometers would be extremely difficult and inefficient. Instead, having a swarm of satellites forming a virtual radar dish offers the advantage of eliminating the structural flexing issues of the large dish structure and the related aiming difficulties.

If the objective of the navigated spacecrafts is to perform a rendez-vous maneuver, the formation flying period of the two vehicles is much smaller than the lifetime of the vehicle itself, since this kind of maneuver generally occurs in one or two orbits. Therefore, as far as the control is concerned, if the description of the relative orbit contains some

minor simplifying assumptions, since the feedback control laws are robust enough, there will be just a small impact on the control performance and the spacecraft will be guided safely to perform the dock maneuver. Moreover, as the two spacecrafts get closer to each other, the relative distance decreases. Thus, the errors introduced into the relative motion description can be neglected during the final instants of this phase.

However, the spacecraft formation flying problem of maintaining the relative orbit of a cluster of satellites is way more sensitive to relative orbit modeling errors than the formation flying problem where two or more vehicles are docking. Making linearizing assumptions can potentially lead to a considerable increase in the fuel consumption. This is caused by the fact that this formation is supposed to be maintained over the whole lifetime of the spacecrafts. Therefore, if a relative orbit is designed using a very simple orbit model, then the formation control laws have to constantly offset these modeling errors burning fuel, that depending on the severity of the modeling errors could dramatically shorten the lifetime of the spacecraft formation. This extreme sensitivity to the orbital dynamics makes this specific kind of formation flying problem very intriguing from the celestial mechanics standpoint [3].

The type of spacecraft formations contemplated in the present research are mostly a cluster of equal satellites. The focus of formation flying is to allow satellites to fly in formation using advanced positioning and control loop technology. Multiple spacecraft flying in a specific geometry enable the formation to reconfigure, adapt baselines, acquire targets and avoids the technical and financial challenge of building one satellite of equivalent size [4]. Moreover, in case of failure of one satellite, it is easier to replace one of the spacecrafts during the mission instead of repairing a subsystem of a big assembly in space [5].

1.2.1 Formation Flying Missions

In recent years, swarms of microsatellites became an attractive alternative to traditional large spacecrafts and several formation flying missions have been conceived, some of which have remained just a concept or a study case, while others have reached the development and operational phase. The main goals of these missions are scientific and programmatic, such us sparse-aperture imaging of extra-solar planets or lunar gravitometry. Spacecraft formation flying have given an increasing scientific return creating new opportunities because of their adaptability to the change of mission objectives. Nevertheless, the current state-of-the-art in control, measurement and modeling of spacecraft formation flying have made some of the proposed missions too expensive. Therefore, in the past few years several proposed formation flying missions have been canceled or transformed into technology-demonstration missions. Currently, there are not so many operational missions involving a large number of spacecrafts in formation, but some operational missions require some technologies and methods to maintain the spacecrafts in formation. Thus, they can be considered spacecrafts formation flying missions. Hereafter some examples of past, present, and future formation flying mission are provided.

TechSat-21

A revolutionary space architecture of collaborating similar spacecrafts was the TechSat-21 (Technology Satellite of the 21st century) concept developed by the U.S. Air Force

Research Laboratory's Space Vehicles Directorate to test technology for formation flight of spacecrafts which can rapidly change formation based on mission requirements. It was supposed to fly three satellites in a near circular orbit at an altitude of approximately $550\ km$. During the mission lifetime the cluster of satellites will fly in various configurations with relative separation distances of approximately $100\ m$ to $5\ km$. One of the objectives of TechSat-21 is to assess the utility of the space-based, sparse-array aperture formed by the satellite cluster. For TechSat-21, the sparse array will be used to synthesize a large radar antenna [6]. The main advantage was the reliability of the system, since a possible loss of one of the spacecrafts could be compensated by the remaining ones preventing the end of the mission. However, the project was canceled in 2003 due to numerous cost overruns.

Cluster

The Cluster mission was first proposed in November 1982 and was ready for launch in 1996. It is a constellation of four spacecraft flying in formation around the Earth into large and highly elliptical polar orbits with perigee and apogee altitudes of respectively $19\,000\ km$ and $119\,000\ km$ [7]. The main goal of the mission is to study the small-scale plasma structures in three dimensions in key plasma regions, such as the solar wind, bow shock, magnetopause, polar cusps, magnetotail and the auroral zones [8]. These spacecrafts fly in a tetrahedral formation carrying identical sets of eleven instruments to investigate charged particles, electrical and magnetic fields.

GRACE

Another mission that implements a formation flying technology is the GRACE (Gravity Recovery And Climate Experiment) mission. It was a joint mission of NASA and the German Aerospace Center (DLR). The mission consisted of two identical satellites GRACE-A and GRACE-B in a leader/follower formation and they were launched together on 17 March 2002 and finished on 27 October 2017 when the spacecrafts ran out of fuel [9]. The objective of the mission was to generate high-fidelity modeling of Earth's gravitational field. A secondary experiment that the GRACE mission performed was investigating how the atmosphere affects GPS signals [2]. The initial altitude of GRACE-A and GRACE-B above the Earth's surface was close to $500\ km$ and it decreased to about $300\ km$ towards the end of the mission because of the atmospheric drag.

PRISMA

The first real mission designed to study spacecraft formation flying was PRISMA (Prototype Research Instruments and Space Mission technology Advancement). It was a technology mission primarily aiming at the demonstration of different sensor technologies and guidance navigation strategies for rendez-vous and formation flying in space. The mission consisted of two spacecraft, one advanced and highly maneuverable called Mango, and one called Tango. Mango was equipped with several sensor systems for formation flying and rendezvous purposes such as GPS, a vision based camera and a radio frequency based navigation instrument together with advanced guidance, navigation and control algorithms. Several high level demonstrations were performed successfully [10]. The satellites were launched from Yasny in Russia on 15 June 2010 to a sun-synchronous orbit at $700\ km$ altitude by a Russian Dnepr rocket.

Proba-3

The Proba-3 mission will provide an opportunity to validate metrology and actuation techniques and technologies, as well as develop and dynamically verify the guidance strategies and navigation and control algorithms required for formation flying during future science, astronomy, and Earth observation missions. It will also test a variety of command and control methodologies and provide development and verification tools and facilities [11]. It consists of two small spacecrafts, launched together in 2024 into a highly elliptical orbit, that will separate apart to fly in tandem, to prepare for future multi-satellite missions flying as one virtual structure [12]. The relative positions of the two craft are determined by S-band radio metrology, which functions for separations between $5\ m$ and $8\ km$, with an accuracy of a few centimeters. Increased accuracy for separations up to $500\ m$ will be obtained using optical laser techniques having both coarse and fine sensors to refine the relative position measurements to an accuracy of hundreds of microns [11].

LISA

The LISA (Laser Interferometer Space Antenna) mission will consist of three spacecrafts separated by 2.5 millions of kilometers in a equilateral triangular formation, following Earth in its orbit around the Sun [13]. These three spacecraft relay laser beams back and forth between the different spacecraft and the signals are combined to search for gravitational wave signatures that come from distortions of spacetime. A giant detector bigger than the size of Earth is necessary to catch gravitational waves from orbiting black holes millions of times more massive than our Sun [14]. The launch of LISA is expected in 2037. The spacecrafts are designed by ESA while NASA will provide the launcher to put them into orbit. LISA Pathfinder spacecrafts were launched in 2015 to help test technologies that will be used in the three LISA spacecrafts.

Swarm

The first constellation mission for Earth observation by ESA is Swarm. The mission consists of three identical satellites named Alpha, Bravo, and Charlie, which were launched on 22 November 2013 into a near-polar orbit, two of which fly side-by-side in identical circular orbits and a third in a higher circular orbit. The objective of the mission is to make the most precise measurements of the Earth's magnetic field ever taken resulting in a survey of the overall geomagnetic field and how it evolves over time [15], as well as the electric field in the atmosphere, by using a satellite constellation that carries sophisticated magnetometers and other instruments. The initial constellation of the mission was achieved on 17 April 2014. Swarm A and C form the lower pair of satellites flying side-by-side (1.4° separation in longitude at the equator) at an altitude of $462\ km$ and at 87.35° inclination angle, whereas Swarm B is cruising at a higher orbit of $511\ km$ and at 87.75° inclination angle. Due to the subtle difference in altitude and inclination, the Swarm B orbit drifts slowly away from the Swarm A and the Swarm C orbits at a rate of about $24^\circ/year$ [16]. The mission is still operating.

SunRISE

The SunRISE (Sun Radio Interferometer Space Experiment) mission consists of six identical spacecrafts with a 6U CubeSat form factor forming an observatory in a 25-hour

circular orbit slightly above GEO to study solar activity [17]. The mission will observe low radio frequency emissions so scientists can understand better how the Sun is able to generate intense space weather storms, known as solar particle storms, that can be hazardous to spacecrafts and astronauts. The SunRISE spacecrafts will orbit within $10\ km$ of one another well above Earth's atmosphere to act like a giant single-aperture radio telescope [18]. The constellation of small spacecraft uses a method known as interferometry, in which many smaller radio telescopes can be combined to mimic a single, much larger observatory with a very high resolving power.

1.2.2 Guidance, Navigation & Control algorithm

The Guidance, Navigation & Control (GNC) subsystem plays a fundamental role since it allows the spacecrafts in the swarm to achieve and keep a given formation imposed by the mission objectives. In such a mission concept, in which the spacecrafts have to react autonomously to unexpected events, a high-level of autonomy and thus an increased complexity is essential. In particular, the collision avoidance task is critical in formation reconfiguration especially when the number of spacecrafts in the swarm increases.

The GNC algorithms can be developed following a centralized, decentralized or distributed architecture. In the centralized architecture there is a master spacecraft processing the information coming from all the other spacecrafts, evaluates the guidance and control results and sends back commands to each spacecraft in the swarm. In the decentralized architecture each spacecraft is capable of computing its own action based solely on on-board information, and the same algorithm is implemented on-board each spacecraft. Finally, the distributed architecture employs inter-satellite links, in fact each spacecraft processes its own information and at least one is coming from another agent of the swarm [19].

The centralized architecture has two main drawbacks: the presence of the master spacecraft indicates a single point failure that will compromise the entire mission, in addition, since the results of the central on-board computation have to be sent to the other agents of the swarm, a further complexity in the communication link between the master spacecraft and all the other spacecrafts is introduced. The decentralized architecture fixes the single failure point aspect, but each spacecraft is limited to its own information. As a consequence, the chosen architecture in this thesis work is the distributed one.

It is important to have an algorithm that can be implemented in a distributed architecture with low computational power, that can handle the collision avoidance actively between more than two spacecrafts and obstacle not related to the swarm. The intended contribution of this thesis work is therefore to propose an autonomous formation reconfiguration GNC algorithm based on Artificial Potential Field, including a distributed active collision avoidance appropriate for microsatellite applications. A feedback controller guarantees that the artificial potential dynamics is followed. A numerical tool in a Matlab-Simulink environment is developed to validate the performance of the algorithm.

The algorithm workflow is the following:

- Acquisition of states measurement by each spacecraft;
- Determination of the relative neighboring states (position and velocity);

- Calculation of the Artificial Potential Field and the corresponding gradient to determine the forced reconfiguration dynamics on-board each spacecraft based on the relative measurements;
- Evaluation of the control effort, subject to thrust constraints, on-board each satellite;
- Determination of the new states using the spacecraft dynamics.

A more detailed description of the algorithm is presented in Section 4.1 supported by a schematic block diagram representing the Simulink model.

1.3 Thesis overview

This thesis work is presented as reported by the following chapters:

Chapter 2: introduces the necessary theoretical background for the implementation of an orbital simulator. It gives a description of the reference frames involved for the development of position dynamics equations which are subsequently derived. Lastly, the most common disturbing forces are presented.

Chapter 3: provides the theory behind the implementation of both the guidance algorithm and the control algorithm. In particular, for the guidance algorithm the Artificial Potential Field method is presented. On the other hand, as far as the control algorithm is concerned the PID family controllers are introduced.

Chapter 4: presents the model developed on a Matlab-Simulink environment and shows the final results of the simulations. Initially, the simulation setup are discussed, which is the desired formation at which the swarm of spacecrafts should aim and the initial conditions for the spacecrafts. Then, five different scenarios are analyzed considering also the presence of fixed and moving obstacles in the space environment that the spacecrafts should avoid, a reconfiguration scenario and a proximity operation scenario. Each simulation is supported by appropriate diagrams showing if the goal was reached and some comments and engineering considerations are made.

Chapter 5: draws the conclusions. Some possible enhancements fixing some of the issues of the proposed approach are also discussed.

Chapter 2

Spacecraft dynamics

To test and demonstrate the effectiveness of the guidance algorithm, spacecraft dynamics has to be taken into account to simulate the motion of the spacecrafts around the Earth. Hence, before the actual design of the Guidance Navigation & Control subsystem, an orbital simulator must be implemented. For the description of the orbital motion is necessary to define some reference frames and to employ the proper differential equations.

In general, the motion of a rigid spacecraft in space is completely defined by four quantities: position, velocity, attitude and angular velocity. However, in this thesis work the last two quantities, describing the rotational motion of the spacecraft about the center of mass, are not taken into account. Therefore, the focus will be on the first two quantities, describing the translational motion of the center of mass of the spacecraft, as a consequence the spacecrafts will be considered as point masses.

In this chapter, the theoretical basis for the realization of the orbital simulator that is been developed on Matlab and Simulink are shown.

2.1 Reference frames

The purpose of this section is to define the reference frames that have been used to describe the orbital motion, for absolute and relative trajectories. Each frame $\mathbf{F}_i$ is defined by its origin $\mathbf{O}_i$ and a set of three orthogonal vectors $\mathbf{a}_1$, $\mathbf{a}_2$, $\mathbf{a}_3$. In [20] it is shown that in general three types of coordinate frames are needed:

- *Orbit reference frames:* to describe the orientation of the orbit relative to inertial space to the Earth and to describe the motion of a spacecraft within an orbit;
- *Spacecraft local orbital reference frames:* to describe the motion relative to a particular point in orbit or to another spacecraft;
- *Spacecraft attitude and body frames:* to describe dynamics and kinematic processes of the spacecraft relative to its center of mass and to describe features relative to the geometry and to a particular point of the spacecraft.

2.1.1 Earth-Centered Inertial Frame

The *Earth-Centered Inertial Frame* ($\mathbf{F}_{ECI}$) is an Earth centered frame whose orientation is fixed in space, thus it is not fixed to the Earth. However, it revolves around the Sun but not around the fixed stars, neglecting the precession of the equinoxes.

In Figure 2.1 the reference frame is illustrated and it is defined as follow:

- The $\mathbf{X}_{ECI}$ axis, with unit vector given by $\hat{I}$, lies in the equatorial plane and points toward the vernal equinox;
- The $\mathbf{Z}_{ECI}$ axis, with unit vector given by $\hat{K}$, normal to the equatorial plane and pointing north;
- The $\mathbf{Y}_{ECI}$ axis, with unit vector given by $\hat{J}$, lies in the equatorial plane, such that $\mathbf{Z}_{ECI} = \mathbf{X}_{ECI} \times \mathbf{Y}_{ECI}$;
- The origin $\mathbf{O}_{ECI}$ is the center of the Earth.

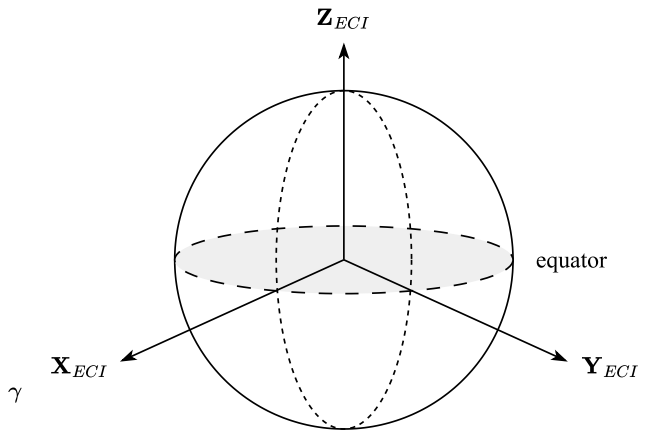

Figure 2.1: *Earth-Centered Inertial Frame*

This reference frame will be used hereafter to apply Newton's second law of motion since it is an inertial reference frame.

2.1.2 Orbital Plane Frame

The *Orbital Plane Frame* ($\mathbf{F}_{op}$) is an Earth centered frame and it is used when the only motion to be described is the one within the orbital plane.

In Figure 2.2 the reference frame is illustrated and it is defined as follow:

- The $\mathbf{x}_{op}$ axis lies in the orbital plane and points toward the ascending node;
- The $\mathbf{z}_{op}$ axis is normal to the orbital plane and inclined to the north direction by the angle i representing the inclination of the orbit;
- The $\mathbf{y}_{op}$ axis lies in the orbital plane and defined such that complete the right-handed system ($\mathbf{z}_{op} = \mathbf{x}_{op} \times \mathbf{y}_{op}$);

- The origin $\mathbf{O}_{op}$ is the center of the Earth.

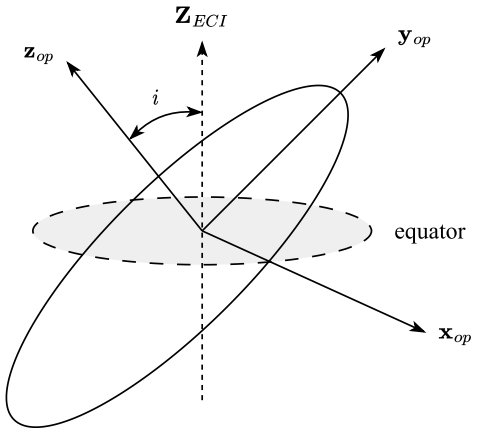

Figure 2.2: *Orbital Plane Frame*

2.1.3 Spacecraft Local Orbital Frame

The *Spacecraft Local Orbital Frame* ($\mathbf{F}_o$) is used to describe the motion with respect to the moving position and direction towards the center of the Earth of an orbiting body.

In Figure 2.3 the reference frame is illustrated and it is defined as follow:

- The $\mathbf{y}_o$ axis is normal to the orbital plane and points in the opposite direction of the angular momentum of the orbit;
- The $\mathbf{z}_o$ axis points to nadir (from the center of mass of the spacecraft to the center of the Earth), thus in the opposite direction of the orbit radius measured in the Earth-Centered Inertial Frame;
- The $\mathbf{x}_o$ axis is defined such that complete the right-handed system ($\mathbf{z}_o = \mathbf{x}_o \times \mathbf{y}_o$);
- The origin $\mathbf{O}_o$ is the center of mass of the spacecraft.

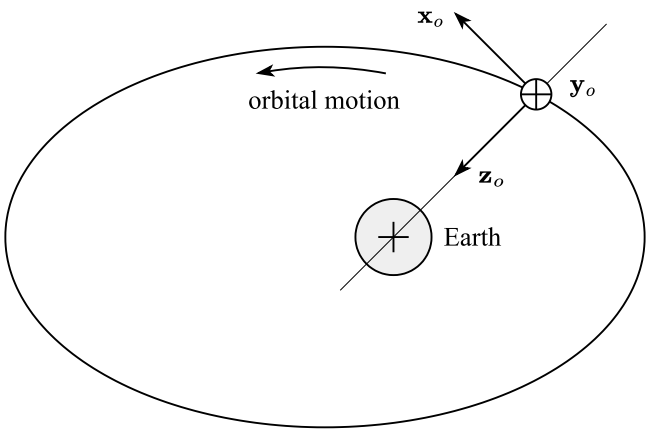

Figure 2.3: *Spacecraft Local Orbital Frame*

This reference frame may be used to describe the orientation of a spacecraft in relation to the Earth surface.

2.1.4 Local-Vertical-Local-Horizontal Frame

The *Local-Vertical-Local-Horizontal Frame* ($\mathbf{F}_{LVLH}$) is a spacecraft local orbital frame for circular orbits. In this instance the $\mathbf{x}_o$ axis is aligned with the orbital velocity vector.

The reference frame is defined as follow:

- The $\mathbf{Y}_{LVLH}$ axis, also known as $\mathbf{H}_{bar}$, is normal to the orbital plane and points in the opposite direction of the angular momentum of the orbit;
- The $\mathbf{Z}_{LVLH}$ axis, also known as $\mathbf{R}_{bar}$, points to nadir, thus in the opposite direction of the orbit radius measured in the Earth-Centered Inertial Frame;
- The $\mathbf{X}_{LVLH}$ axis, also known as $\mathbf{V}_{bar}$, is defined such that complete the right-handed system and points to the same direction of the orbital velocity vector;
- The origin $\mathbf{O}_o$ is the center of mass of the spacecraft.

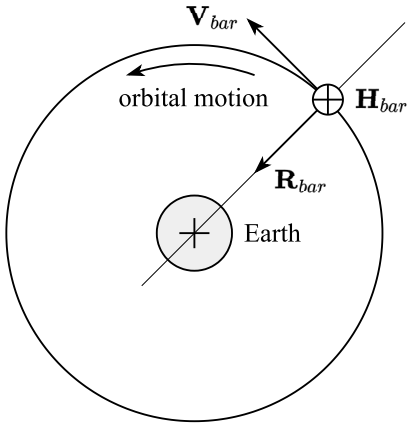

Figure 2.4: *Local-Vertical-Local-Horizontal Frame*

This reference frame will be used to describe the relative motion between the spacecrafts and the target position employing the Hill's equations.

2.2 Position dynamics

In this section the fundamentals of position dynamics are introduced and the Hill's equations will be derived for the description of the orbital motion.

2.2.1 The two-body problem

The problem of determining the motion of two bodies as a result of their own mutual gravitational attraction is defined by the Newton's Law of Universal Gravitation, which

states that any two bodies attract one another with a force proportional to the product of their masses and inversely proportional to the square of the distance between them. This law can be expressed mathematically in vector notation as:

$$\bar{F}_g = -\frac{Gm_1m_2}{r^2}\frac{\bar{r}}{r} \tag{2.1}$$

where $G = 6.67 \cdot 10^{-11}\ m^3kg^{-1}s^{-2}$ is the universal gravitational constant, m_1 and m_2 are the masses of the two bodies, and $\bar{r}$ is a vector whose magnitude r is given by the distance between the two bodies.

To determine the equation of relative motion of these two bodies, two simplifying assumptions will be made with regard to the model:

1. The bodies are spherically symmetric. This way the two bodies may be treated as though their masses were concentrated at their centers;

2. There are neither external nor internal forces acting on the system except for the gravitational forces acting along the line joining the centers of the two bodies.

Before applying the Newton's second law, as suggested by [21] and [22], an inertial reference frame must be found in order to measure the motion or the lack of it. For this purpose the Earth-Centered Inertial Frame can be chosen.

Through some straightforward steps the vector differential equation of the relative motion for the two-body problem can be derived:

$$\ddot{\bar{r}} = -\frac{G(m_1 + m_2)}{r^2}\frac{\bar{r}}{r} \tag{2.2}$$

Assuming that $m_1 = M$ is the mass of the Earth and $m_2 = m$ is the mass of the spacecraft and neglecting the mass of the spacecraft with respect to the one of the Earth follows that:

$$G(M + m) \approx GM \tag{2.3}$$

It is convenient to define a parameter given by the product of the universal gravitational constant and the mass of the main body, called gravitational parameter. For the Earth:

$$\mu \equiv GM = 3.986 \cdot 10^5\ km^3s^{-2} \tag{2.4}$$

As a consequence Equation 2.2 can be written as:

$$\ddot{\bar{r}} = -\frac{\mu}{r^2}\frac{\bar{r}}{r} \tag{2.5}$$

This equation will be used hereafter to describe the relative dynamics and derive Hill's equation. Also, it is common to define a state vector containing six elements, the first three of them represent the position and the last three of them the velocity of the spacecraft. Deriving in time the state vector it is possible to obtain the velocity and the acceleration of the spacecraft given by Equation 2.5. Conversely, by integrating the components of this vector the position and the velocity of the spacecraft can be obtained.

2.2.2 Hill's equations

Let us consider two bodies, the target (**T**) and the chaser (**C**). For each of the two bodies it is possible to define a vector representing the position of the body with respect to the origin of the chosen reference frame. If the Orbital Plane Frame is used for this purpose, then the magnitude of this vector represents also the distance between the body and the center of the Earth.

Since it is convenient to describe the relative dynamics of the chaser with respect to the target a new vector $\bar{s}$ is defined, representing the relative dynamics vector. An illustration of the above is shown in Figure 2.5.

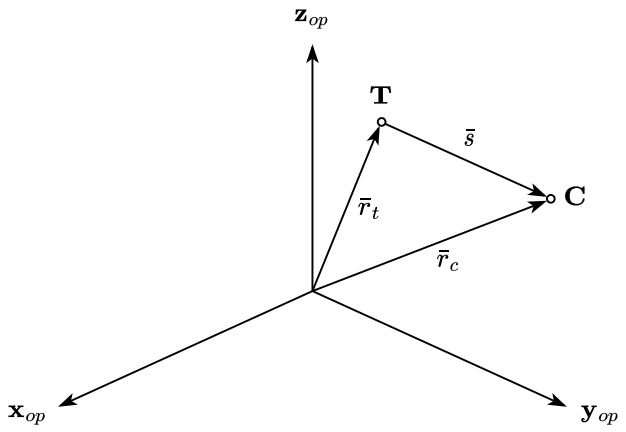

Figure 2.5: *Relative dynamics vector representation*

This can be expressed mathematically in vector notation as:

$$\bar{s} = \bar{r}_c - \bar{r}_t \tag{2.6}$$

As far as the target is concerned the free restricted two body (FR2B) problem is considered, hence, the only force acting on the target is the gravitational force of the Earth.

$$\bar{F}_g(\bar{r}_t) = m_t \ddot{\bar{r}}_t = -m_t \frac{\mu}{r_t^3} \bar{r}_t \tag{2.7}$$

From which the acceleration measured in the inertial reference frame can be derived:

$$\bar{f}_g(\bar{r}_t) = \ddot{\bar{r}}_t = -\frac{\mu}{r_t^3} \bar{r}_t \tag{2.8}$$

Where r_t is a vector identifying the position of the target given by the sum of the radius of the Earth and the altitude of the target orbit:

$$r_t = r_\oplus + h_t \tag{2.9}$$

On the other hand, as far as the chaser is concerned the restricted two body (R2B) problem is considered, hence, in addition to the gravitational force also a generic force, taking into account external perturbation, is contemplated.

$$\bar{F}_g(\bar{r}_c) + \bar{F} = m_c \ddot{\bar{r}}_c = -m_c \frac{\mu}{r_c^3} \bar{r}_c + \bar{F} \tag{2.10}$$

From which the acceleration measured in the inertial reference frame can be derived:

$$\bar{f}_g(\bar{r}_c) + \bar{f}(\bar{r}_c) = \ddot{\bar{r}}_c = -\frac{\mu}{r_c^3} \bar{r}_c + \frac{\bar{F}}{m_c} \tag{2.11}$$

Once both the accelerations of target and chaser are defined, it is possible to obtain the relative acceleration of the chaser w.r.t. the target deriving in time Equation 2.6 twice.

$$\ddot{\bar{s}} = \ddot{\bar{r}}_c - \ddot{\bar{r}}_t \tag{2.12}$$

Therefore, substituting Equation 2.8 and Equation 2.11 into Equation 2.12 one has that:

$$\ddot{\bar{s}} = \bar{f}_g(\bar{r}_c) - \bar{f}_g(\bar{r}_t) + \frac{\bar{F}}{m_c} \tag{2.13}$$

To develop the difference between the gravitational acceleration of chaser and target the acceleration of the chaser must be linearized using a first order Taylor expansion centered on the radius of the target:

$$\bar{f}_g(\bar{r}_c) = \bar{f}(\bar{r}_c) + \left.\frac{d\bar{f}_g(\bar{r})}{d\bar{r}}\right|_{\bar{r}=\bar{r}_t} (\bar{r}_c - \bar{r}_t) \tag{2.14}$$

Where $\bar{r}$ is a vector whose components are:

$$\bar{r} = \left[r_x \, , \, r_y \, , \, r_z\right]^T \tag{2.15}$$

Whose magnitude is:

$$r = |\bar{r}| = \sqrt{(r_x^2 + r_y^2 + r_z^2)} \tag{2.16}$$

The derivative of the vector function $\bar{f}_g$ with respect to the vector $\bar{r}$ can be defined through the Jacobian matrix $\mathbf{M}$. The form of the vector function $\bar{f}_g$ is given by:

$$\bar{f}_g(\bar{r}) = -\frac{\mu}{r^3} \bar{r} = \left[-\frac{\mu}{r^3} r_x \, , \, -\frac{\mu}{r^3} r_y \, , \, -\frac{\mu}{r^3} r_z \right] \tag{2.17}$$

The diagonal elements of the Jacobian matrix, with $i = j$ are:

$$\frac{\partial \bar{f}_g(r_i)}{\partial r_i} = -\mu \left[r^{-3} - 3\, r^{-5} r_i^2\right] = -\frac{\mu}{r^3} \left[1 - 3\, \frac{r_i^2}{r^2}\right] \tag{2.18}$$

The extra-diagonal elements of the Jacobian matrix, with $i \neq j$ are:

$$\frac{\partial \bar{f}_g(r_i)}{\partial r_i} = -\mu \left[-3\, r^{-5} r_i r_j\right] = -\frac{\mu}{r^3} \left[3\, \frac{r_i r_j}{r^2}\right] \tag{2.19}$$

Thus, considering the difference between the vector functions $\bar{f}_g(\bar{r}_c)$ and $\bar{f}_g(\bar{r}_c)$ one has:

$$\bar{f}_g(\bar{r}_c) - \bar{f}_g(\bar{r}_t) = \left.\frac{d\bar{f}_g(\bar{r})}{d\bar{r}}\right|_{\bar{r}=\bar{r}_t} (\bar{r}_c - \bar{r}_t) = -\frac{\mu}{r^3}\,\mathbf{M}\,\bar{s} \tag{2.20}$$

Where the Jacobian matrix $\mathbf{M}$ is given by:

$$\mathbf{M} = \begin{bmatrix} 1 - 3\,\dfrac{r_x^2}{r_t^2} & 3\,\dfrac{r_x r_y}{r_t^2} & 3\,\dfrac{r_x r_z}{r_t^2} \\ 3\,\dfrac{r_y r_x}{r_t^2} & 1 - 3\,\dfrac{r_y^2}{r_t^2} & 3\,\dfrac{r_y r_z}{r_t^2} \\ 3\,\dfrac{r_z r_x}{r_t^2} & 3\,\dfrac{r_z r_y}{r_t^2} & 1 - 3\,\dfrac{r_z^2}{r_t^2} \end{bmatrix} \tag{2.21}$$

Ultimately, the relative acceleration vector become:

$$\ddot{\bar{s}} = -\frac{\mu}{r^3}\,\mathbf{M}\,\bar{s} + \frac{\bar{F}}{m_c} \tag{2.22}$$

Equation 2.22 represents the relative motion of the chaser with respect to the target in the Orbital Plane Frame, which is an inertial frame. Now the goal is to represent this motion in a different reference frame that is the Spacecraft Local Orbital Frame, that considering circular orbits is the Local-Vertical-Local-Horizontal Frame.

The second derivative of the vector $\bar{s}$ in the Orbital Plane Frame is given by:

$$\frac{d^2\bar{s}}{dt^2} = \frac{d^2\bar{s}^*}{dt^2} + \frac{d^2\bar{\omega}}{dt^2} \times \bar{s}^* + \bar{\omega} \times (\bar{\omega} \times \bar{s}^*) + 2\,\bar{\omega} \times \frac{d\bar{s}^*}{dt} = -\frac{\mu}{r^3}\,\mathbf{M}\,\bar{s} + \frac{\bar{F}}{m_c} \tag{2.23}$$

Where $\bar{s}$ is measured in the Orbital Plane Frame and its components are:

$$\bar{s} = [\mathbf{x}_{op}\,,\,\mathbf{y}_{op}\,,\,\mathbf{z}_{op}]^T \tag{2.24}$$

While $\bar{s}^*$ is measured in the LVLH Frame and its components are:

$$\bar{s}^* = [x\,,\,y\,,\,z]^T \tag{2.25}$$

In Equation 2.23 considering the terms on the second member, the first term represents the acceleration measured in the LVLH Frame, namely the relative acceleration, the second and the third terms represent respectively the tangential and normal acceleration of the LVLH Frame with respect to the Orbital Plane Frame and the fourth term represents the Coriolis acceleration.

Also, in the Local-Vertical-Local-Horizontal Frame one has that:

$$\bar{\omega} = [0\,,\,-\omega\,,\,0]^T \tag{2.26}$$

$$\bar{r}_t = [0\,,\,0\,,\,-r_t]^T \tag{2.27}$$

Developing the terms in Equation 2.23 one has that:

$$\begin{Bmatrix} \ddot{x} \\ \ddot{y} \\ \ddot{z} \end{Bmatrix} + \begin{Bmatrix} -\dot{\omega}z \\ 0 \\ \dot{\omega}x \end{Bmatrix} + \begin{Bmatrix} -\omega^2 x \\ 0 \\ -\omega^2 z \end{Bmatrix} + \begin{Bmatrix} -2\omega\dot{z} \\ 0 \\ 2\omega\dot{x} \end{Bmatrix} = - \begin{Bmatrix} \omega^2 x \\ \omega^2 y \\ -2\omega^2 z \end{Bmatrix} + \frac{\bar{F}}{m_c} \tag{2.28}$$

It can be demonstrated that the angular velocity ω coincides with the orbital angular velocity in a circular orbit, thus, it is a constant equal to:

$$\omega = \sqrt{\frac{\mu}{r_t^3}} \tag{2.29}$$

Since the angular velocity ω is a constant, its derivative in time is equal to zero. Therefore, the following scalar equations can be obtained:

$$\begin{cases} \ddot{x} = \dfrac{F_x}{m_c} + 2\omega\dot{z} \\ \ddot{y} = \dfrac{F_y}{m_c} - \omega^2 y \\ \ddot{z} = \dfrac{F_z}{m_c} - 2\omega\dot{x} + 3\omega^2 z \end{cases} \tag{2.30}$$

They are the so-called Hill's equations describing the position dynamics for circular orbits in the Local-Vertical-Local-Horizontal Frame. They can be employed when the distance between chaser and target is much smaller than the radius of the orbit.

The components of the vector $\bar{F}$ are given by a term that takes into account the forces applied to the chaser by the actuation system, for example the thrusters, and a term that includes all the other external disturbances or perturbations:

$$\begin{cases} F_x = F_{x,th} + F_{x,ex} \\ F_y = F_{y,th} + F_{y,ex} \\ F_z = F_{z,th} + F_{z,ex} \end{cases} \tag{2.31}$$

2.3 Perturbations

Studying and modeling perturbations are key disciplines in astrodynamics. It is crucial to have some mathematical models for each perturbing force. These can be analytical formulas, or even tabular representations (e.g. tables of atmospheric density). In this section the most common disturbing forces are presented. In general, external perturbations act both on the position and on the attitude of the spacecraft, however, in this thesis work just the ones acting on the position are taken into account.

External disturbances usually have a small magnitude with respect to internal disturbances, for this reason they do not have a great impact on the motion of the spacecraft in the short term. However, these perturbations are persistent, so they can't be neglected in

the long term. Furthermore, these perturbations depends on the altitude of the orbit. In the simulations are analyzed both scenarios in Geostationary Earth Orbit (GEO) and Low Earth Orbit (LEO). In GEO it is assumed that there are not external perturbations, while in LEO the only perturbing forces considered are the atmospheric drag and the J2 effect.

2.3.1 Atmospheric drag

Drag is caused by atmospheric particles, which interacting with the satellite decelerate its motion. In LEO there is still some trace of atmospheric particles, however, the atmosphere is so rarefied that the conventional fluid mechanics theories based on a continuum model of the atmosphere are not applicable. Therefore, the interaction between the spacecraft and the atmosphere must be treated at the molecular level.

Let us consider the following assumption:

- The momentum of molecules impacting the spacecraft is totally lost to its surface;
- The thermal motion of the atmosphere is much smaller than the spacecraft speed;
- The spacecraft is nominally non-spinning.

The basic equation for aerodynamic drag is given by the following equation:

$$\bar{f}_d = -\frac{1}{2}\,\rho\, v_{rel}^2 \left(\frac{C_D\, A}{m}\right) \frac{\bar{v}_{rel}}{v_{rel}} \tag{2.32}$$

where ρ is the atmospheric density at the satellite altitude and it is perhaps the most difficult parameter to determine. It was evaluated using the exponential atmospheric model which assumes that the density of the atmosphere decays exponentially with increasing altitude. It also assumes a spherically symmetrical distribution of particles. According to this model the density is given by:

$$\rho = \rho_0\, \exp\left[\, -\frac{h_{ellp} - h_0}{H}\right] \tag{2.33}$$

where ρ_0 is the reference density, h_0 is the reference altitude, h_{ellp} is the actual altitude above the ellipsoid and H is the scale height. In Figure 2.6 the values of the atmospheric density from 100 to 1000 km are shown. These values are taken from [23] and are calculated considering the U.S. Standard Atmosphere (1976) [24].

Considering again Equation 2.32, v_{rel} is the relative velocity of the spacecraft with respect to the atmosphere. C_D is the coefficient of drag and it is a dimensionless quantity which reflects the susceptibility of the spacecraft to drag forces. For spacecrafts in the upper atmosphere it is often considered constant and equal to 2.2 (using a flat plate model).

Finally, A is the cross-sectional area of the spacecraft and m represents its mass. Together with the coefficient of drag these three terms inside the brackets in Equation 2.33 represents the inverse of the ballistic coefficient which measures the ability of a body to overcome air resistance in flight. With this definition, a low ballistic coefficient means the spacecraft will be affected by drag a lot - and vice versa.

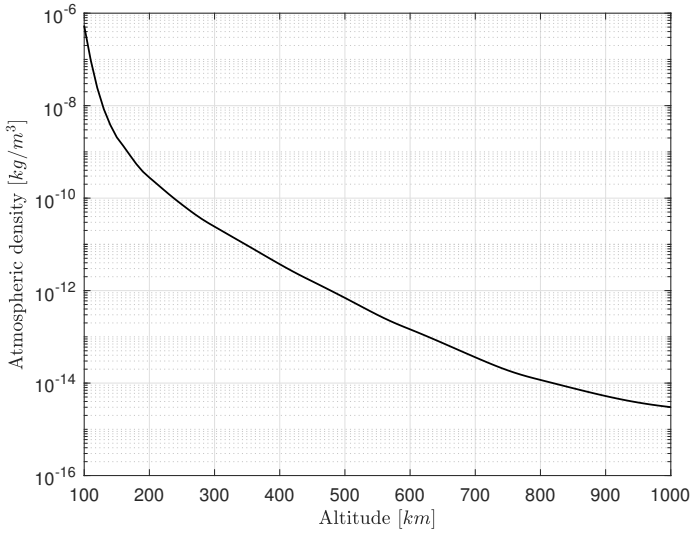

Figure 2.6: *Exponential Atmospheric Model*

2.3.2 J_2 effect

The term J_2 comes from an infinite series mathematical equation that describes the perturbational effects of oblation on the gravity of a planet. The coefficients of each term in this series is described as J_k, of which J_2, J_3 and J_4 are called zonal coefficients. However, J_2 is over 1000 times larger than the rest and has the strongest perturbing factor on orbits.

A formulation of the perturbation force for the J_2 effect is given by:

$$\bar{F}_{J_2} = -m \frac{3\, J_2\, \mu\, r_\oplus}{2\, r^4} \begin{bmatrix} 1 - 3\sin^2 i\ \sin\nu \\ 2\sin^2 i\ \sin\nu\ \cos\nu \\ 2\sin i\ \cos i\ \sin\nu \end{bmatrix} \tag{2.34}$$

where m is the mass of the spacecraft, J_2 is a constant, μ is the gravitational parameter of the Earth, $r_\oplus$ is the radius of the Earth, r is the radius of the orbit, i is the inclination of the orbit and ν is the true anomaly.

In general the force related to this perturbation is not a constant since the true anomaly is a parameter that varies in time. To simplify the evaluation the terms into the square parenthesis are not taken into account since these terms do not affect the order of magnitude of this orbital disturbance. Then, this perturbation is evaluated as a force acting along the three axes with the same intensity. In vector notation:

$$\bar{F}_{J_2} = -m \frac{3\, J_2\, \mu\, r_\oplus}{2\, r^4} \begin{bmatrix} 1 \\ 1 \\ 1 \end{bmatrix} \tag{2.35}$$

Such force perturbs just the position of the spacecraft without affecting its attitude.

Chapter 3

Guidance and control algorithm

This thesis work draws inspiration from a navigation scheme to perform the acquisition maneuvers and the formation keeping of the swarm of spacecrafts called Equilibrium Shaping (ES) technique. Such a decentralized navigation scheme is characterized by an extreme simplicity, as a consequence it is very suitable for the path planning and control for a complex and coupled system such as a swarm of spacecrafts. The resulting navigation scheme seem particularly flexible since the ES technique can be considered as a two level approach decoupling the path planning and the control feedback definition.

The objective is therefore to build a real time navigation scheme giving to each agent of the swarm the capability to decide autonomously what final target to acquire knowing just the position of all the members of the swarm, and to safely navigate towards it without conflicting with the other spacecrafts.

A two-step approach is considered: first, a method is developed that for the desired formation defines for each member of the swarm the desired velocity vector as a sum of different weighted contributions named behaviors, then, a control technique is considered allowing each agent of the swarm to track the desired kinematical field. In this way the control design is totally independent from the design of the desired velocity field, for that reason it will be faced separately.

3.1 Equilibrium Shaping Technique

In this section a brief introduction to the mathematical modeling used for the ES technique is presented following closely what shown in [25], [26] and [27]. This approach draws inspiration from past published works on robot path planning and artificial intelligence. This technique consists in building a dynamical system that has as equilibrium points all the possible agents permutations in the final target formation, this dynamical system is then used to derive the desired velocities for all the agents in the swarm.

The dynamic is designed as a sum of three different behavior named: *gather*, *avoid* and *dock*. The mathematical expression of each kind of behavior along with a brief description of its meaning are listed below:

- **Gather Behavior:** This behavior introduces N different global attractors towards

the N targets. The analytical expression of the i^{th} agent desired velocity given by this behavior contribution can be written in the following form:

$$\dot{\bar{x}}_i^{gather} = \sum_{j=1\,,\,j\neq i}^{N} c_j\,\psi_G(\|\bar{\xi}_j - \bar{x}_i\|)(\bar{\xi}_j - \bar{x}_i) \tag{3.1}$$

where ψ_G is a mapping from positive reals to positive reals that introduces some non linear dependency from the target distance. Letting the c_j coefficient to depend solely on the targets position and not on the specific member it is possible to make sure that each agent of the swarm is identical to the others so that the behavior is not affected by the agent permutations. The function ψ_G depends only on the distance.

- **Dock Behavior:** This behavior introduces N different local attractors towards the N targets. The analytical expression of the i^{th} agent desired velocity given by this behavior contribution can be written in the following form:

$$\dot{\bar{x}}_i^{dock} = \sum_{j=1\,,\,j\neq i}^{N} d_j\,\psi_D(\|\bar{\xi}_j - \bar{x}_i\|\,,\,k_D)(\bar{\xi}_j - \bar{x}_i) \tag{3.2}$$

  The component of this desired velocity field has a non-negligible value only if the agent of the swarm is in the neighborhood of the sink. The parameter k_D is related to the radius of the sphere of influence of the dock behavior. The function ψ_D is a mapping from positive reals to positive reals that goes to zero outside a given radius from the target. What has been said for the c_j coefficient is true also for the d_j coefficient since the dock behavior is similar to the gather behavior except that it is a local attractor and not a global one, thus it rules the final docking procedure.

- **Avoid Behavior:** This behavior settle a relationship between two different members of the swarm that are relatively close to each other. The analytical expression of the i^{th} agent desired velocity given by this behavior contribution can be written in the following form:

$$\dot{\bar{x}}_i^{avoid} = \sum_{j=1\,,\,j\neq i}^{N} b\,\psi_A(\|\bar{x}_i - \bar{x}_j\|\,,\,k_A)(\bar{x}_i - \bar{x}_j) \tag{3.3}$$

  The component of this desired velocity represents a repulsive force. The function ψ_A is a mapping from positive reals to positive reals that goes to zero whenever the distance between the two agents of the swarm is considered not dangerous according to the k_A parameter. Since a symmetry between all the members of the swarm has to be maintained the b parameter is independent by the particular agent.

As stated before, the desired velocity field for a swarm of N agents and for a desired formation is therefore defined by the following expression:

$$\dot{\bar{x}}_i = \dot{\bar{x}}_i^{gather} + \dot{\bar{x}}_i^{dock} + \dot{\bar{x}}_i^{avoid} \tag{3.4}$$

This builds a dynamical system defined by the weighted sum of different behaviors.

3.2 Artificial Potential Field

In this section some of the results relevant to this study for the autonomous path planning technology using APF method developed in [1] and [28] are summarized.

3.2.1 Path planning using APF

Let us consider a continuous time synchronous swarm model consisting of N individuals (members) in the n dimensional Euclidean space. The position in space of the i^{th} individual is defined by $x_i \in \mathbb{R}^n$. It is assumed that synchronous motion exists, so all the agents of the swarm can change their position in space at the same time, and there is no time delay.

Under these assumptions the motion dynamics of each of the swarm members is ruled by the following law:

$$\dot{\bar{x}}_i = \sum_{j=1\,,j\neq i}^{N} \bar{g}(\bar{x}_i - \bar{x}_j) \qquad i = 1, \ldots, N \tag{3.5}$$

where $\bar{g} : \mathbb{R}^n \to \mathbb{R}^n$ is an odd function given by the sum of the attraction and repulsion functions between the agents of the swarm. The function $\bar{g}$ can be expressed as:

$$\bar{g}(\bar{y}) = \bar{y}\left[g_a(\|\bar{y}\|) - g_r(\|\bar{y}\|)\right] \tag{3.6}$$

where $\bar{y} \in \mathbb{R}^n$ is an arbitrary vector and $\|\bar{y}\|$ is its Euclidean norm given by:

$$\|\bar{y}\| = \sqrt{\bar{y}^T\bar{y}} \tag{3.7}$$

Another way to represents Equation 3.5 is the following:

$$\dot{\bar{x}}_i = -\nabla_{\bar{x}_i} J(\bar{x}) \qquad i = 1, \ldots, N \tag{3.8}$$

where $J : \mathbb{R}^{nN} \to \mathbb{R}$ is an artificial potential function determining the attraction/repulsion relationship between the swarm members, while $\bar{x}$ represents the position vector of all the individuals in the swarm. The potential function $J(\bar{x})$ is not static and depends solely on the relative positions of the agents in the swarm.

Let us consider an artificial potential function of the form:

$$J(\bar{x}) = \sum_{i=1}^{N-1} \sum_{i=i+1}^{N} J_{ij}(\|\bar{x}_i - \bar{x}_j\|) \tag{3.9}$$

where $J_{ij}(\|\bar{x}_i - \bar{x}_j\|)$ is the value of the potential between the agent i^{th} and the agent j^{th} and can be different for different pairs. Furthermore, it is assumed that it satisfies the following conditions:

1. The potentials $J_{ij}(\|\bar{x}_i - \bar{x}_j\|)$ are symmetric and satisfy:

$$J_{ij}(\|\bar{x}_i - \bar{x}_j\|) = -J_{ij}(\|\bar{x}_i - \bar{x}_j\|) \tag{3.10}$$

2. There exist functions $J_a^{ij} : \mathbb{R}^+ \to \mathbb{R}^+$ and $J_r^{ij} : \mathbb{R}^+ \to \mathbb{R}^+$ such that:

$$J_{ij}(.) = J_a^{ij}(.) - J_r^{ij}(.) \tag{3.11}$$

$$\nabla_y J_a(\|\bar{y}\|) = \bar{y}\, g_a^{ij}(\|\bar{y}\|) \tag{3.12}$$

$$\nabla_y J_r(\|\bar{y}\|) = \bar{y}\, g_r^{ij}(\|\bar{y}\|) \tag{3.13}$$

where $J_a(\|\bar{y}\|)$ and $J_r(\|\bar{y}\|)$ are respectively the attractive potential function that dominates on long distances and the repulsive potential function that dominates on short distances. The two just mentioned assumptions restrict the motion of the individuals toward each other along the gradient of these potentials (i.e. along the combined gradient field of these potentials).

3. There exists unique distance δ_{ij} at which:

$$g_{ar}^{ij}(\delta_{ij}) = g_a^{ij}(\delta_{ij}) - g_r^{ij}(\delta_{ij}) = 0 \tag{3.14}$$

$$g_{ar}^{ij}(\|\bar{y}\| > \delta_{ij}) > 0 \tag{3.15}$$

$$g_{ar}^{ij}(\|\bar{y}\| < \delta_{ij}) < 0 \tag{3.16}$$

Then, δ_{ij} is the unique distance at which attraction and repulsion balance each other, as a consequence:

$$g_a^{ij}(\delta_{ij}) = g_r^{ij}(\delta_{ij}) \tag{3.17}$$

Any function satisfying the above assumptions results in aggregating swarm behavior. Assuming that the motion of the agents of the swarm is given by Equation 3.5 it can be demonstrated that the following assumptions are true.

1. The center of the swarm is stationary for all time:

$$\bar{x}_{mean} = \frac{1}{N} \sum_{i=1}^{N} \bar{x}_i = const. \tag{3.18}$$

2. If $J(\bar{x})$ is bounded from below, i.e. $J(\bar{x}) > a$ for some $a \in \mathbb{R}$, then for any initial conditions $\bar{x}(0) \in \mathbb{R}^{nN}$, as $t \to \infty$ we have $\bar{x}(t) \to \Omega_e$, where $\Omega_e = \{\bar{x} : \dot{\bar{x}} = 0\}$.

3. The size of the swarm will be bounded and the position i^{th} of each individual of the swarm will converge asymptotically to a small region around its center $\bar{x}_{mean}$, which is an hyperball of size ε:

$$B_\varepsilon(\bar{x}) = \{\bar{y} \,:\, \|\bar{y} - \bar{x}_{mean}\| \leqslant \varepsilon\} \tag{3.19}$$

   Moreover, the convergence to B_ε will occur in a finite time.

Despite given the initial positions of the members of the swarm, the final configuration to which the individuals will converge is unique, a direct relation between $\bar{x}(0)$ and $\bar{x}(\infty)$ is difficult to find, therefore this is a shortcoming of this approach.

Under the just mentioned assumptions about the potential function Equation 3.5 with the pair dependent attraction/repulsion becomes:

$$\dot{\bar{x}}_i = \sum_{j=1\,,\,j\neq i}^{N} \bar{g}_{ij}(\bar{x}_i - \bar{x}_j) \qquad i = 1,\,\ldots,\,N \tag{3.20}$$

where $\bar{g}_{ij} \,:\, \mathbb{R}^n \to \mathbb{R}^n$ is the attraction/repulsion function that for all pairs $(i\,,\,j)$ satisfies:

$$\bar{g}_{ij}(\bar{x}_i - \bar{x}_j) = -\bar{g}_{ij}(\bar{x}_j - \bar{x}_i) \tag{3.21}$$

For formation control the attraction and repulsion functions and with them the equilibrium distance δ_{ij} for different pairs of individuals can be different.

To specify the desired formation uniquely with respect to translation and rotation for all the pairs $(i\,,\,j)$ with $j \neq i$ the formation constraints $\|\bar{x}_i - \bar{x}_j\| = d_{ij}$ can be used, choosing each of the attraction/repulsion functions $\bar{g}_{ij}(.)$ such that for every pair of individuals $(i\,,\,j)$ one has that $\delta_{ij} = d_{ij}$.

The generalized Lyapunov function is given by:

$$J(\bar{x}) = \sum_{i=1}^{N-1} \sum_{i=i+1}^{N} \left[J_a^{ij}(\|\bar{x}_i - \bar{x}_j\|) - J_r^{ij}(\|\bar{x}_i - \bar{x}_j\|)\right] \tag{3.22}$$

It has its minimum at the desired formation and once the formation is achieved $\bar{x}_i = 0$ for all i. If $J(\bar{x})$ is chosen as a formation function, with the just mentioned characteristics, then the desired configuration will be achieved asymptotically.

The potential function considered for formation control that satisfies these assumptions is the function with linear attraction and exponential repulsion terms shown in Figure 3.1 whose mathematical expression is given by:

$$\bar{g}(\bar{y}) = -\bar{y}\left[a - b\,\exp\left(-\|\bar{y}^2\|/c\right)\right] \tag{3.23}$$

where a, b and c are positive constants such that $b > a$. The constant a represents the magnitude of the attraction, b represents the magnitude of the repulsion and c represents

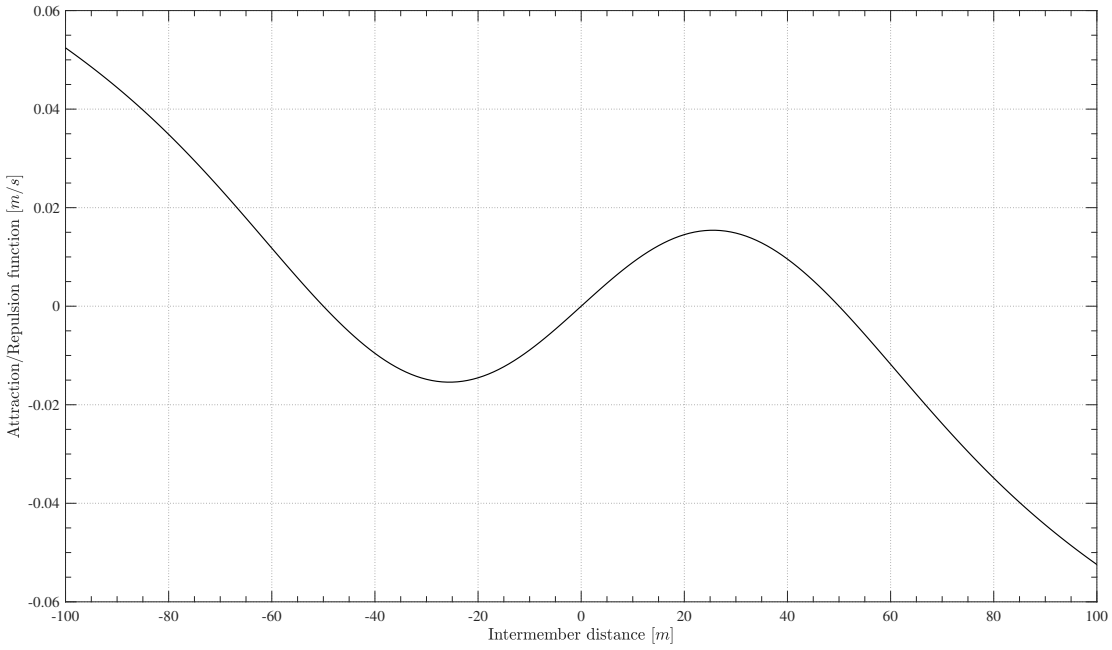

Figure 3.1: *Attraction/Repulsion function*

its spread or repulsion range. However, the actual repulsion is given by some combination from effects of both. In particular a is defined by:

$$a = b \, \exp\left(-d^2/c\right) \tag{3.24}$$

This parameter is evaluated so that a balance of attraction and repulsion between any two agents is achieved at the desired distance d in the final tetrahedron formation. The collision avoidance can be guaranteed by increasing the parameter b that in turn increases the repulsive force.

By equating Equation 3.23 to zero, it is clear that the potential function switches sign at the set of points defined by $\Psi = \{\|\bar{y}\| = 0 \cup \|\bar{y}\| = \delta = sqrt(c/\ln(b/a))\}$. From the plot of the potential function in Figure 3.1 can be seen that it crosses the horizontal axis at the desired formation separation that is the distance at which attraction balance the repulsion.

3.2.2 Spacecraft navigation using APF

The schematic diagram of path planning and control architecture used in this thesis work is shown in Figure 3.2. The purpose of the path planning module is to avoid obstacles and to provide a goal-oriented navigation in an optimal time period. In the Artificial Potential Field (APF) method, the dynamic environment in which the spacecraft exists is described by a scalar potential function. This function is shaped so that the minimum potential, representing the sink, is placed at the desired terminal state of the vehicle dynamics and the maximum potential, representing the source, is placed in the path constrains, such us obstacles or other spacecrafts. Therefore, each spacecraft in the swarm represents a region of high potential. Letting the repulsive force be in the opposite direction of the gradient

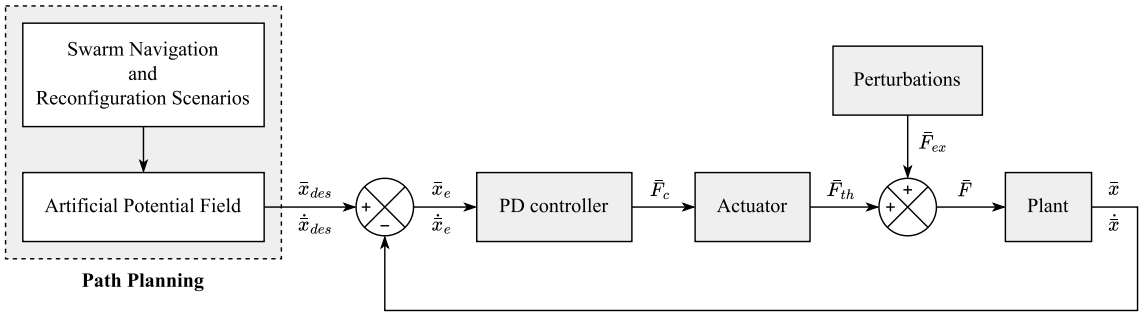

Figure 3.2: *Schematic diagram of path planning and control, adapted from [1]*

of the potential field, the collision between the neighboring spacecrafts is avoided.

The Artificial Potential Field method guides the spacecraft towards the desired terminal state without violating the defined path constraints. This is guaranteed by the fact that the rate of descent of the potential function is rendered negative definite. The final formation is achieved only if every member of the swarm is in a sink corresponding to the target configuration. If compared to deliberative techniques carrying out extensive map building from raw sensory data, this approach has a way less computational load.

In Figure 3.3 it is shown how the Artificial Potential Field method works, in particular which are the forces experienced by a spacecraft belonging to the swarm. In this example three spacecrafts are considered (Swarm Agent 1, Swarm Agent 2 and Swarm Agent 3) and it is desired that the Swarm Agent 2 moves starting from its current position towards the target position avoiding the collision with the other members of the swarm. In the first step Swarm Agent 1 exerts a repulsive force ($\bar{F}_{rep1}$) on Swarm Agent 2, while the target exerts an attractive force ($\bar{F}_{att1}$). As a result Swarm Agent 2 moves in a new location in the direction of the resulting force ($\bar{F}_{t1}$). In this new position, Swarm Agent 3 exerts a repulsive force ($\bar{F}_{rep2}$) on Swarm Agent 2, and once again the target exerts an attractive force ($\bar{F}_{att2}$). The vector sum of the two forces ($\bar{F}_{t2}$) guides Swarm Agent 2 towards the next new location. This procedure is repeated until Swarm Agent 2 reaches its target position, thereby achieving the final desired configuration.

In this proposed approach the next location of the Swarm Agent is therefore determined by assuming that all the other agents in the swarm are obstacles and exert repulsive forces on it, while the target position (desired terminal state) asserts an attractive force. As a consequence, the spacecraft is driven towards the goal or the desired terminal state by a generalized force given by the negative of the total potential gradient. Therefore, the Artificial Potential Field method provides a constantly active navigation that allows the spacecrafts in a swarm to achieve the desired formation with a collision free trajectory.

In this thesis work the above mentioned theory is used to allow the spacecraft swarm to achieve the desired formation. However, after the occurrence of the PD controller the center of the formation $\bar{x}_{mean}$ is expected to be almost stationary. As a consequence, the position of the final configuration on orbit will depend on the initial position of each member in the swarm. Therefore, if the desired center of the formation is not the initial one, the desired velocity field must be modified to drive the whole formation towards a

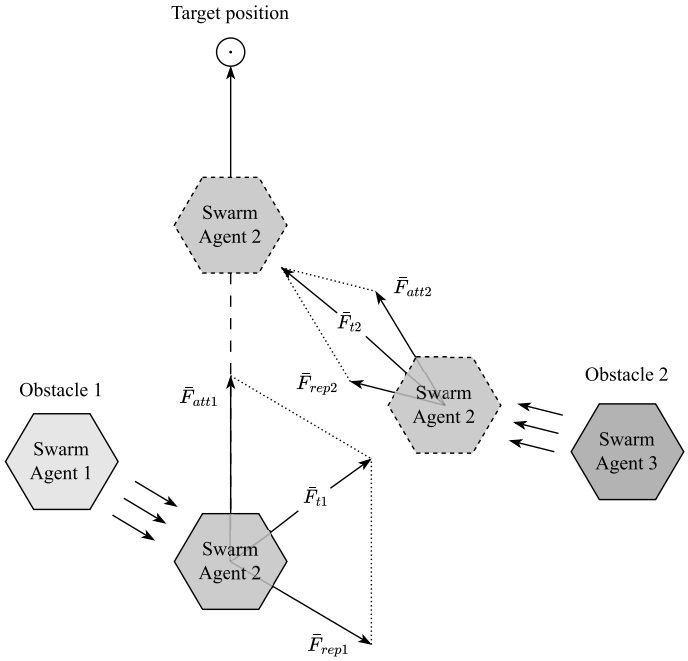

Figure 3.3: *Schematic diagram of path planning using APF, adapted from [1]*

specific point on orbit. In addition, the repulsion considered in this approach is purely between the members of the swarm, thus an interaction with an object not belonging to the swarm is not contemplated. Hence, a further component in the desired velocity field is introduced to take into account a possible collision with such an obstacle. The mathematical expression of the desired velocity field is thus given by:

$$\dot{\bar{x}}_i = \dot{\bar{x}}_i^{swarm} + \dot{\bar{x}}_i^{cos} + \dot{\bar{x}}_i^{obs} \tag{3.25}$$

The first term in Equation 3.25 represents the desired velocity developed in Equation 3.5, the expressions of the second and the third terms will be developed in the next sections, following closely the approach developed in [29], [30] and [31].

3.2.3 Attractive Potential Field

To guide the whole swarm towards the desired location on orbit a paraboloid artificial potential field is considered. It is a stabilizing function since the desired velocity decrease as the spacecraft approach the target position. The mathematical expression of the attractive potential field is given by:

$$U_{att}(\bar{x}_{mean}) = \frac{1}{2}\, k_{att} \left\| \bar{x}_{mean} - \bar{x}_{mean}^{des} \right\|^2 \tag{3.26}$$

where k_{att} is the proportional positive gain of the attractive gradient, while $\bar{x}_{mean}$ is the center of the swarm defined by Equation 3.18. It can be noticed that the attractive potential field depends solely on the position of the center of the swarm and not on the position of each member of the swarm since it can be demonstrated that the center of the swarm is stationary for all time during the maneuver should this additional attractive potential field not be applied. Therefore, the value of the attractive potential field is the same for all the members of the swarm as if they should move towards the desired location rigidly

without moving w.r.t. each other. Thus, a rigid translation is expected for all the agents.

The gradient of the attractive potential field is given by the following expression:

$$\nabla U_{att}(\bar{x}_{mean}) = k_{att}\left(\bar{x}_{mean} - \bar{x}_{mean}^{des}\right) \tag{3.27}$$

where the term inside the parenthesis represents the vector that points from the desired position of the center of the swarm to its current position. The component of the desired velocity that attracts the whole swarm towards the desired position on orbit is given by the negative gradient of the attractive potential field as follows:

$$\dot{\bar{x}}_i^{cos} = -\nabla U_{att}(\bar{x}_{mean}) \tag{3.28}$$

In Equation 3.28 there is a negative sign due to the fact that the spacecrafts should move towards the areas with a lower potential.

3.2.4 Repulsive Potential Field

In order to assure collision avoidance with obstacles an hyperbolic artificial potential field is built around each obstacle. The mathematical expression of the repulsive potential field is given by:

$$U_{rep,i}(\bar{x}_i) = \begin{cases} \frac{1}{2}\, k_{rep}\left(\frac{1}{\rho(\bar{x}_i)} - \frac{1}{\rho_0}\right)^2 & : \quad \rho(\bar{x}_i) \leqslant \rho_0 \\ 0 & : \quad \rho(\bar{x}_i) \geqslant \rho_0 \end{cases} \tag{3.29}$$

where k_{rep} is the proportional positive gain of the repulsive gradient, while $\rho(\bar{x}_i)$ is a scalar parameter whose value is given by the magnitude of the vector pointing from the center of the obstacle to the spacecraft subtracted by the radius of the obstacle as shown in the following expression:

$$\rho(\bar{x}_i) = \|\bar{x}_i - \bar{x}_{obs}\| - r_{obs} \tag{3.30}$$

where $\bar{x}_i$ is a vector defining the position of the i^{th} agent of the swarm, $\bar{x}_{obs}$ is a vector defining the position of the obstacle, both measured in the Local-Vertical-Local-Horizontal Frame, while r_{obs} is a scalar parameter representing the radius of the obstacle.

Lastly, ρ_0 is a scalar parameter representing the distance from the surface of the obstacle, on which the repulsive potential field tends to infinity, to the surface of an imaginary sphere, on which the repulsive potential field goes to zero. It can be seen also as the maximum distance at which a sensor on the spacecraft is able to recognize the presence of an obstacle. Therefore, it is also known as the distance of influence of the obstacle. In Figure 3.4 is shown a graphic representation of the parameters introduced in this section.

As can be seen in Equation 3.29 the repulsive potential field has a non-zero value if the distance from the surface of the obstacle is less than ρ_0, otherwise its value is zero. This means that if the spacecraft is far enough from the surface of the obstacle the presence of the obstacle can be neglected, since knowing the position of obstacles that are too far away from the spacecraft would be unrealistic because their presence is stated by sensors

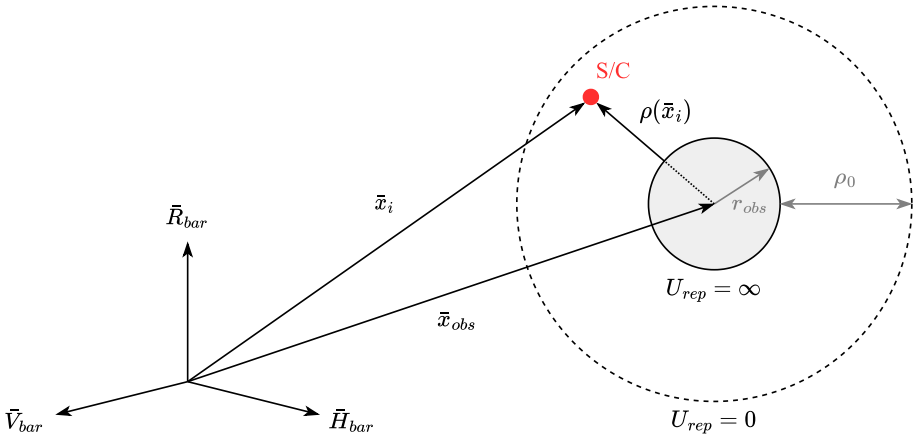

Figure 3.4: *Vectors for defining the repulsive potential*

on board of the spacecraft that have a limited range. The fact that the value of the repulsive potential field goes to zero at a ρ_0 distance from the surface of the obstacle guarantees a continuity of the potential field.

The gradient of the repulsive potential field is given by the following expression:

$$\nabla U_{rep,i}(\bar{x}_i) = \begin{cases} -k_{rep}\left(\dfrac{1}{\rho(\bar{x}_i)} - \dfrac{1}{\rho_0}\right)\dfrac{\nabla\rho(\bar{x}_i)}{\rho(\bar{x}_i)^2} & : \quad \rho(\bar{x}_i) \leqslant \rho_0 \\ 0 & : \quad \rho(\bar{x}_i) \geqslant \rho_0 \end{cases} \tag{3.31}$$

where the gradient of the $\rho(\bar{x}_i)$ parameter is given by:

$$\nabla\rho(\bar{x}_i) = \frac{\bar{x}_i - \bar{x}_{obs}}{\|\bar{x}_i - \bar{x}_{obs}\|} \tag{3.32}$$

The component of the desired velocity that pushes away the single spacecraft of the swarm from the obstacle to guarantee collision avoidance is given by the negative gradient of the repulsive potential field as follows:

$$\dot{\bar{x}}_i^{obs} = -\nabla U_{rep,i}(\bar{x}_i) \tag{3.33}$$

As stated before, in Equation 3.33 there is a negative sign due to the fact that the spacecrafts should move towards the areas with a lower potential.

3.3 Control system design

In the previous sections the guidance algorithm used in this thesis work has been extensively discussed. At this point it is necessary to introduce a control algorithm whose purpose is to generate an input for the actuation system on board of the spacecraft to perform maneuvers and reach the desired position. Fundamentally, in control theory there are two types of control loop: open-loop control (feedforward) and closed-loop control (feedback). They give an elegant and robust solution to many control design problems.

In open-loop control the control action from the controller is independent of the controlled output variable. Therefore, an open-loop controller is used in simple processes because of its simplicity and low cost, especially in systems where feedback is not critical. However, if the system is not so easy to model or some unexpected external perturbations are acting on the system this type of controller is not appropriate to control the system.

In closed-loop control the control action from the controller depends on the controlled output variable. A closed-loop controller is designed to automatically achieve and maintain the desired output condition by comparing it with the actual condition. It does this by generating an error signal which is the difference between the output and the reference input. Their main characteristics are the capability to: reduce the errors by automatically adjusting the input for the system, improve the stability of an unstable system, increase or reduce the system sensitivity, enhance the robustness against external perturbations to the process and produce a reliable and repeatable performance. Whilst a good closed-loop system can have many advantages over an open-loop control system, its main disadvantage is that in order to provide the required amount of control, a closed-loop system must be more complex by having one or more feedback paths. Also, if the gain of the controller is too sensitive to changes in its input commands or signals it can become unstable and start to oscillate as the controller tries to over-correct itself.

3.3.1 PID Controller Structure

A particular control structure that has become almost universally used in industrial control is based on a particular fixed structure controller family, the so-called PID controller family. They have proven to be robust in the control of many important applications [32]. There are four types of controllers that belong to the PID controller family: the proportional controller (P), the proportional plus integral controller (PI), the proportional plus derivative controller (PD) and the proportional plus integral plus derivative controller (PID) [33]. The basic idea of PID control systems is discussed hereafter.

In Figure 3.5 a generic error defined as the difference between the desired output variable and the actual variable is considered. The error is a time dependent signal, so it is possible to evaluate this parameter over time. Furthermore, it is possible to see the time history of the error, measured in terms of integral of the error (highlighted area in the image). The bigger the highlighted area, the bigger the error made in the past. This information can be used to modify the command given to the plant. Another information that can be exploited is the derivative of the error at time t. According to the derivative of the error it is possible to understand if the error is decreasing, increasing or remaining constant depending on whether the derivative is less than zero, greater than zero or equal to zero.

The PID controller can generate a command for the plant based on the value of the error, its integral or its derivative. Their impact on the closed loop is far from independent of each other, their effect was thought as follows:

- **Proportional action:** produces a contribution to the command depending on the instantaneous value of the control error. A proportional controller can control easily any stable plant, but it provides limited performance and nonzero steady state errors.
- **Integral action:** gives a controller output that is proportional to the accumulated

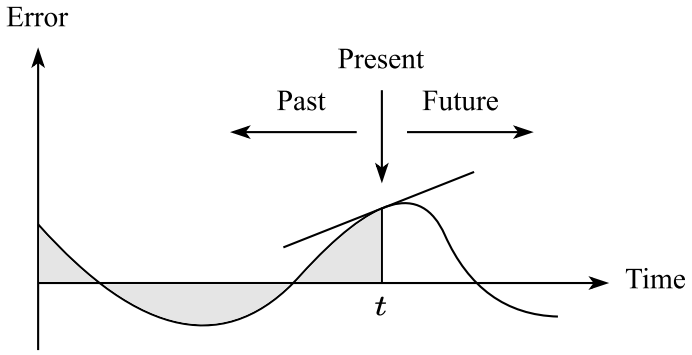

Figure 3.5: *Error in time, idea behind PID controller*

error, which implies that it is a slow reaction control mode. The integral mode plays a fundamental role in achieving perfect plant inversion. This forces the steady state error to zero in the presence of a step reference and disturbance. The integral mode, viewed in isolation, has two major shortcomings: its pole at the origin is detrimental to loop stability and it also gives rise to the undesirable effect (in the presence of actuator saturation) known as wind-up.

- **Derivative action:** acts on the rate of change of the control error. Consequently, it is a fast mode which ultimately disappears in the presence of constant errors. It is sometimes referred to as a predictive mode because of its dependence on the error trend. The main limitation of the derivative mode, viewed in isolation, is its tendency to yield large control signals in response to high frequency control errors, such as errors induced by setpoint changes or measurement noise.

Proportional Controller

The simplest controller is the proportional controller. In this kind of controller the feedback control signal $\bar{u}(t)$ is evaluated in proportion to the feedback error $\bar{e}(t)$ as follows:

$$\bar{u}(t) = K_P\, \bar{e}(t) \tag{3.34}$$

where K_P is the proportional gain, while the feedback error is the difference between the reference signal and the output signal as shown in the following expression:

$$\bar{e}(t) = \bar{x}_{i/des}(t) - \bar{x}_i(t) \tag{3.35}$$

Due to its simplicity, the proportional controller is often used in all those cases when not so much information about the system are available and the required control performance in steady-state operation is not so demanding.

One of the limitations of such a simple controller is that the steady-state error of the closed-loop control system will not be completely eliminated. The controller involves only one parameter to be determined, as a consequence it is possible to choose K_P without too many information about the plant.

Proportional plus Derivative Controller

Most of the time, a proportional controller is not adequate to achieve a specific control purpose such as stabilization or producing damping for the closed-loop system. In these instances, the derivative of the feedback error signal can be taken into account into the control signal calculation as shown in the following expression:

$$\bar{u}(t) = K_P\,\bar{e}(t) + K_D\,\dot{\bar{e}}(t) \tag{3.36}$$

where K_D is the derivative gain, while the derivative of the feedback error is the difference between the derivative of the reference signal and the derivative of the output signal as shown in the following expression:

$$\dot{\bar{e}}(t) = \dot{\bar{x}}_{i/des}(t) - \dot{\bar{x}}_i(t) \tag{3.37}$$

The proportional plus derivative controller permits to decrease the overshoot but it requires more time to reach the desired state.

Proportional plus Integral Controller

Another commonly used controller among the PID family controllers is the proportional plus integral controller. Because of the integral action, the steady-state error existing with the proportional controller alone is totally eliminated. The output of the controller is given by the sum of two terms, one from the proportional action and the other one from the integral action as follows:

$$\bar{u}(t) = K_P\,\bar{e}(t) + K_I\int_0^t \bar{e}(t)\,dt \tag{3.38}$$

where K_I is the integral gain which multiply the integral of the error signal. The output of a proportional integral control system is usually characterized by an overshoot to a step reference signal. On the one hand, a fast control system response is achieved, on the other hand, the percentage of overshoot increases.

Proportional plus Integral plus Derivative Controller

Lastly, the proportional plus integral plus derivative controller consists of three terms: the proportional term, the integral term and the derivative term. The output of the controller is given by the sum of three terms as in the following expression:

$$\bar{u}(t) = K_P\,\bar{e}(t) + K_I\int_0^t \bar{e}(t)\,dt + K_D\,\dot{\bar{e}}(t) \tag{3.39}$$

This controller brings together the characteristics of the previous ones. It can be said that increasing the value of the K_P parameter degrades the stability of the system, decreases the steady-state error, but increases the overshoot. Increasing the value of the K_I parameter degrades the stability of the system, significantly decreases the steady-state error, but increases the overshoot. Finally, increasing the value of the K_D parameter improves the stability of the system and decreases the overshoot.

Chapter 4

Simulations and results

In this chapter the results obtained from the simulations are presented. The simulations where conducted using a three-degree-of-freedom orbital simulator built in a Matlab-Simulink environment. In the first section of this chapter the design of the orbital simulator is briefly presented, while in the following sections the studied scenarios are analyzed.

4.1 Orbital simulator design

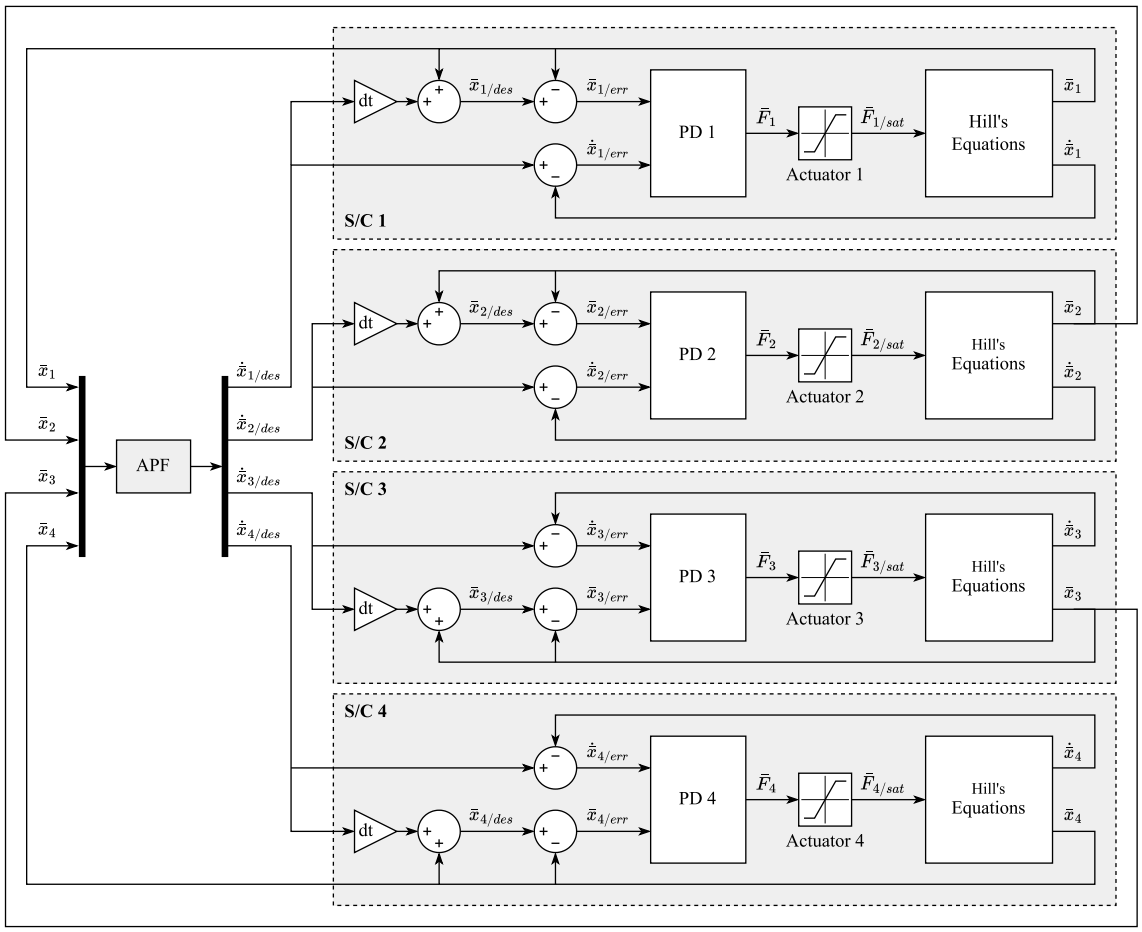

Figure 4.1: *Representative diagram of the orbital simulator*

The representative diagram of the orbital simulator is shown in Figure 4.1. The orbital simulator is constituted by four main elements: the guidance, the controller, the actuators and the plant. Each element is described hereafter.

The guidance is a Matlab function whose inputs are the positions $\bar{x}_i$ of each spacecraft in the swarm measured in the Local-Vertical-Local-Horizontal Frame, hence, it is a twelve-element column vector. It uses these inputs to generate the desired velocity field as explained in section 3.2. The desired velocity $\dot{\bar{x}}_{i/des}$ of each spacecraft in the swarm is then integrated in time to obtain the desired position $\bar{x}_{i/des}$ in that time step. The desired positions and the desired velocities are then compared with the actual ones to obtain respectively the error in the position $\bar{x}_{i/err}$ and the error in velocity $\dot{\bar{x}}_{i/err}$ that serve as inputs for the controller.

The controller is simply a proportional plus derivative (PD) controller that multiplies each of the inputs for a given constant and adds up the results to obtain the theoretical force $\bar{F}_i$ to apply along each of the three axes.

The actuators are modeled by a saturation block on Simulink to take into account the fact that it is not possible to provide any value of thrust, but this is bounded.

Finally, the plant is represented by the Hill's equations which describe the position dynamic of the spacecrafts on orbit measured in the Local-Vertical-Local-Horizontal Frame. Also, in this block, the perturbations given by the atmospheric drag and the J_2 effect acting on the plant are taken into account simply adding the disturbing forces to the control forces provided by the actuators. The output from this block is the state vector given by:

$$\bar{x}_i^{S/C} = \left[\bar{x}_i \, , \, \dot{\bar{x}}_i\right]^T \tag{4.1}$$

where $\bar{x}_i$ and $\dot{\bar{x}}_i$ are respectively the position and the velocity of the i^{th} spacecraft. The state vector, in particular, the positions of each of the members in the swarm are used to evaluate the desired velocity field through the Artificial Potential Field method in the next time step and so on until the end of the simulation. The current velocity field is instead compared with new desired one to obtain a new input for the controller.

4.2 Simulations setup

In order to verify the effectiveness of the algorithm to guide the spacecrafts towards the desired configuration while avoiding obstacles and to evaluate its performance a certain number of simulations were conducted. Five different scenarios were analyzed: in the first one the spacecrafts in the swarm are the only entities in orbit, in the second one a fixed obstacle was also considered, in the third one the obstacle has a certain velocity with respect to the Local-Vertical-Local-Horizontal Frame, in the fourth one the possibility by the swarm to rearrange the formation was evaluated, finally, a proximity operation scenario was taken into account to estimate the maximum dimension of the obstacle that the swarm of spacecrafts can avoid during the formation acquisition maneuver.

In each of the scenarios the initial conditions are evaluated as follows. The initial positions are chosen randomly, the only criteria is that the magnitude of the distance from each

Simulation Parameter	**Value**
Spacecraft mass, m	$14\ kg$
Number of S/C for tetrahedron formation, N	4
Repulsion constant in APF, b	0.0015
Repulsion range constant in APF, c	2500
Final inter spacecraft formation separation, d	$50\ m$
Attraction constant global APF, k_{att}	0.001
Repulsive constant global APF, k_{rep}	1000
Distance of influence of the obstacle, ρ_0	$200\ m$
Proportional gain PD controller, K_p	0.01
Derivative gain PD controller, K_d	1000
Maximum thrust, T_{max}	$0.05\ N$
Orbit radius, r	$42164\ km$

Table 4.1: *Simulation parameters*

spacecraft to the target position should be the same for all the spacecrafts in the swarm, as shown in the following expression:

$$\bar{x}_i^{\,0} = \lambda \frac{\bar{\alpha}_i}{\|\bar{\alpha}_i\|} \tag{4.2}$$

where λ is a constant scalar parameter whose value is equal to the desired distance and it is the same for all the spacecrafts, while $\bar{\alpha}_i$ is a three-component vector whose components are random real numbers between zero and one. In this way it possible to locate the spacecrafts at the proper distance but the direction is chosen randomly.

With regard to the initial velocity, it is imposed to be the one of the free drift motion since the orbit of the target and the one of each spacecraft in the swarm is different:

$$\begin{cases} \dot{x}_i^{\,0} = 3/2\,\omega\, z_i^{\,0} \\ \dot{y}_i^{\,0} = 0 \\ \dot{z}_i^{\,0} = 0 \end{cases} \tag{4.3}$$

where ω is the orbital angular velocity in the circular orbit of the target and it is evaluated as shown in Equation 2.29, while $z_i^{\,0}$ is simply the third component of the initial position vector shown in Equation 4.2. The other two components of the initial velocity are set equal to zero.

In Table 4.1 the simulation parameters are shown with the respective values. As can be seen the orbit chosen to run the simulations is a Geostationary Earth Orbit.

4.3 No obstacle simulation

The first scenario is the simplest one because the spacecrafts of the swarm are the only entities in orbit, therefore, there is an interaction between them but not with other objects external to the swarm. The objective of the guidance algorithm in this case is to achieve the desired formation in the target position on orbit. The desired formation is a tetrahedron formation, which is a regular three-dimensional shape, and the spacecrafts representing the vertexes of the tetrahedron are equidistant from from each other.

In Figure 4.2 the trajectories of the four spacecrafts are represented in the Local-Vertical-Local-Horizontal Frame. The initial positions are illustrated by black circles, the trajectories by a black line, while the red dots represent the final position.

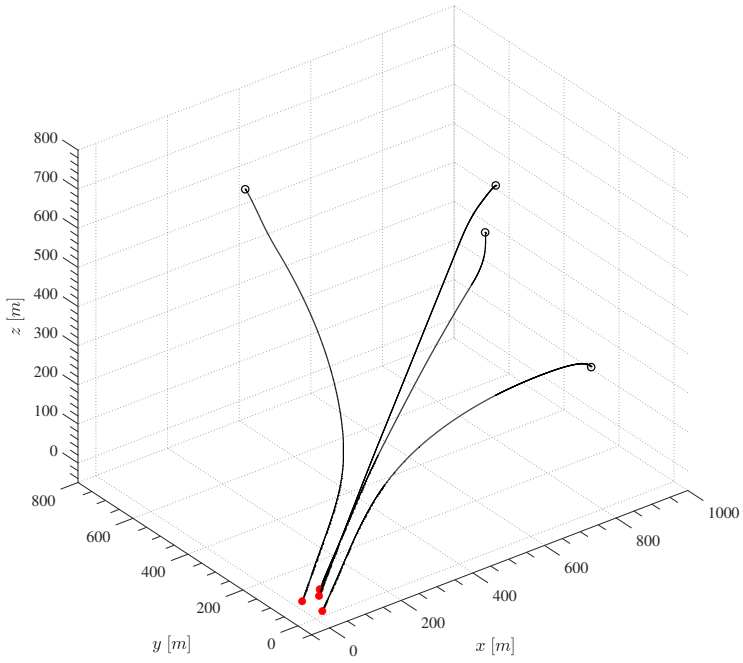

Figure 4.2: *Trajectories of the spacecrafts (no obstacle)*

As can be seen the spacecrafts move towards the target position on orbit and at the same time they attract each other to achieve the desired formation. How much one effect dominates the other can be regulated changing the parameters b and k_{att}. In particular, the b parameter is the repulsion constant in the Artificial Potential Field method concerning the term of the desired velocity that permits the formation to be acquired, so decreasing this term will permit to achieve the formation faster, on the other hand, increasing the k_{att} parameter will allow the center of the formation to reach the target position faster.

In Figure 4.3 a zoom of the tetrahedron formation in shown. Using this approach the final orientation of the tetrahedron in space can't be decided but it depends on the initial condition. In other words, each spacecraft is not attracted towards a specific position since the beginning of the simulation but the desired position changes at each time step depending on how the spacecrafts interact with each other. The center of the swarm is illustrated using the asterisk symbol and it is located in the origin of the axes.

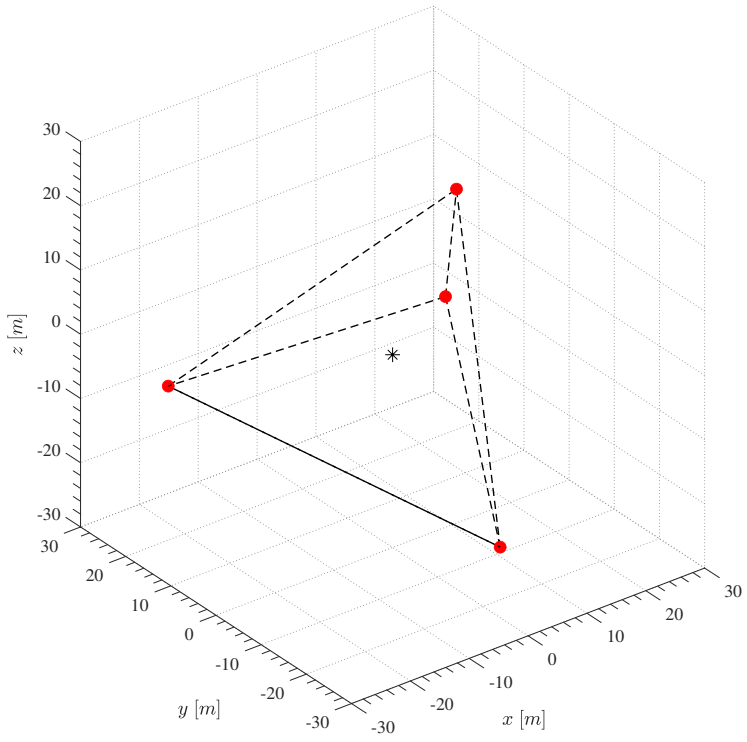

Figure 4.3: *Tetrahedron formation (no obstacle)*

In Figure 4.4 the coordinates of the spacecrafts over time are shown, where each row represents a different spacecraft. In particular, the actual positions are illustrated with a continuous line, while the desired positions with a dashed line. It can be seen that the two lines are basically overlapped, this means that the controller is able to provide the proper command allowing the spacecrafts to follow the desired path.

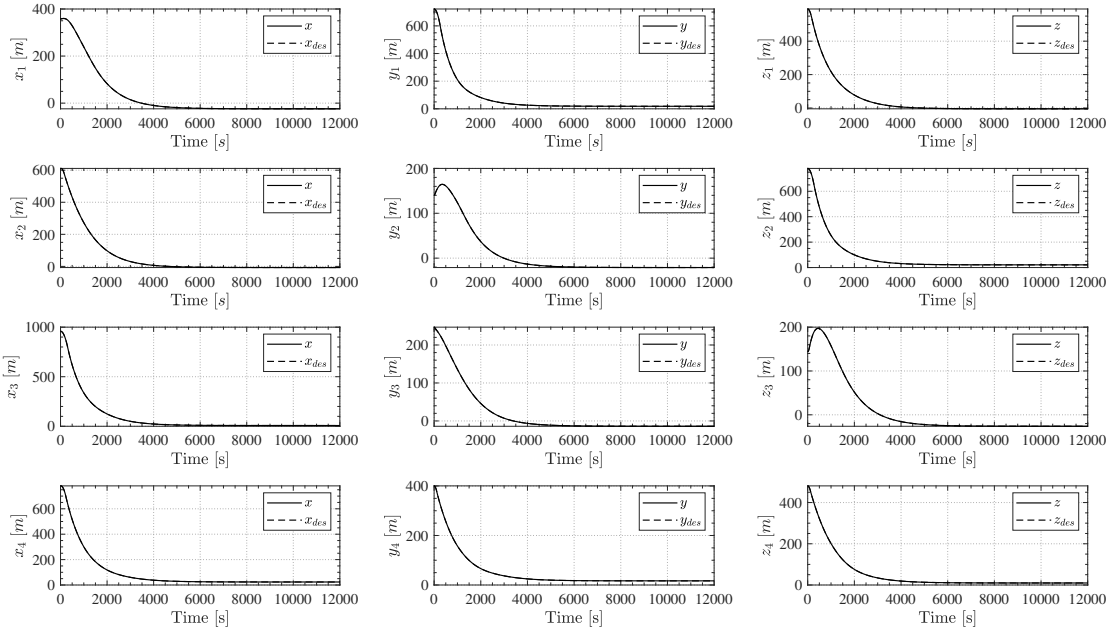

Figure 4.4: *Coordinates of the spacecrafts over time (no obstacle)*

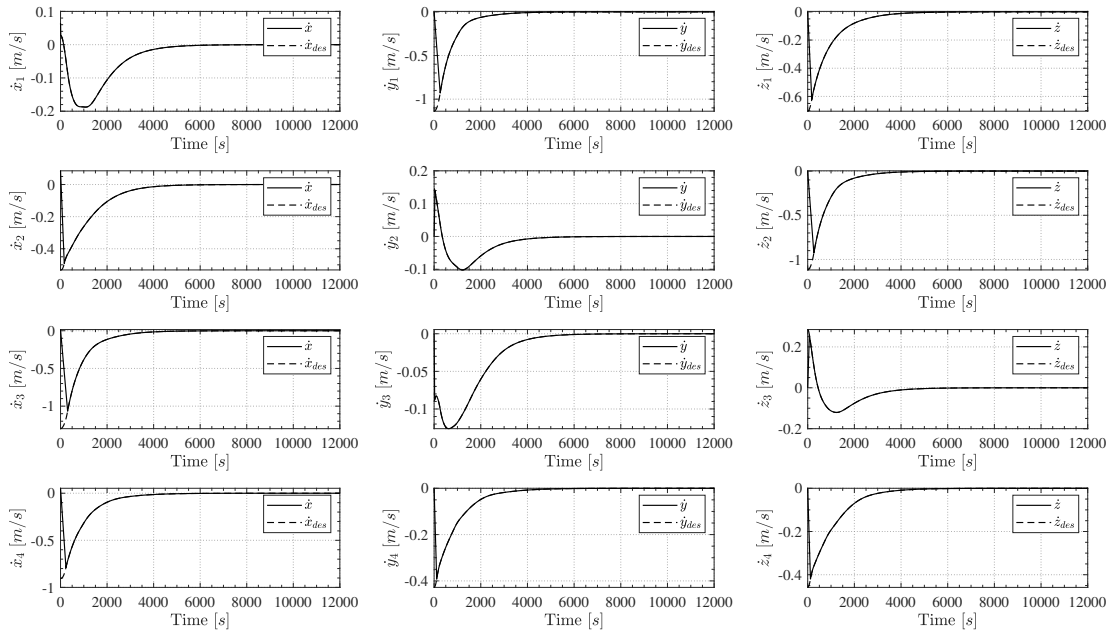

Figure 4.5: *Velocity field of the spacecrafts over time (no obstacle)*

In Figure 4.5 the velocity field of the spacecrafts over time is shown. Both the actual velocities, with a continuous line, and the desired velocities, with a dashed line, are illustrated. As can be seen, in the first few instants of the maneuver the actual velocities are close to zero and not equal to the desired ones because there is a certain delay due to the inertia of the spacecrafts that at the beginning have different velocities from the desired ones. Initially both the actual and the desired velocities increase in magnitude and at the end of the maneuver they approach zero, as they should, to keep the formation.

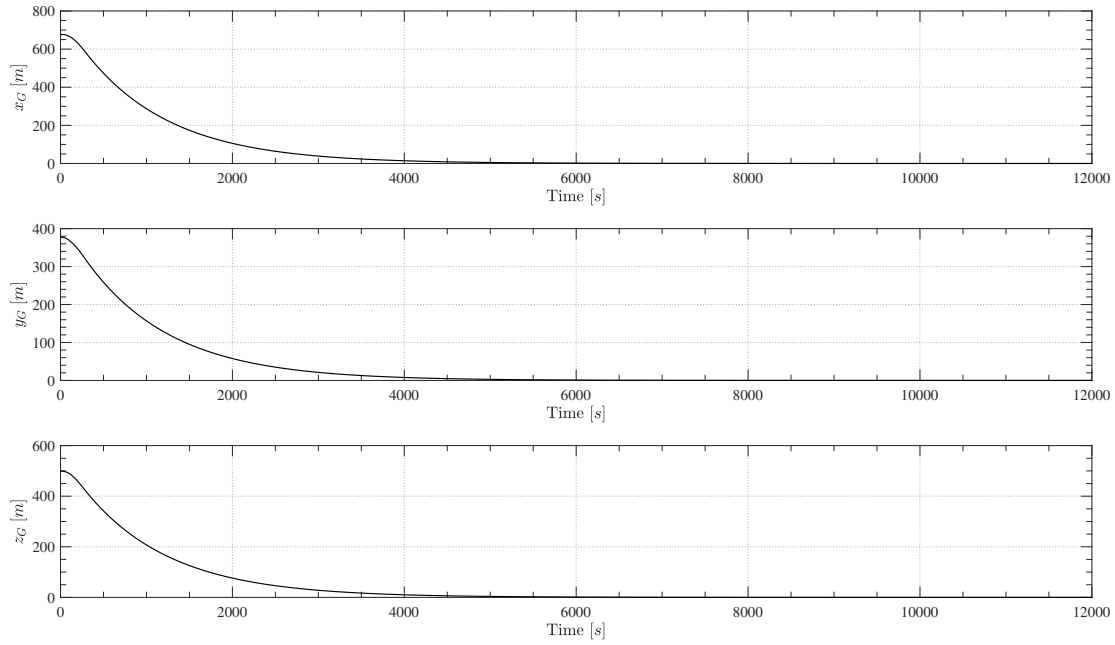

Figure 4.6: *Center of the swarm position over time (no obstacle)*

In Figure 4.6 the center of the swarm position over time is shown. It can be seen that it moves from the initial random position to the origin of the axes. The simulation time is $12000\ s$ but the final configuration is reached in less time in this simple scenario.

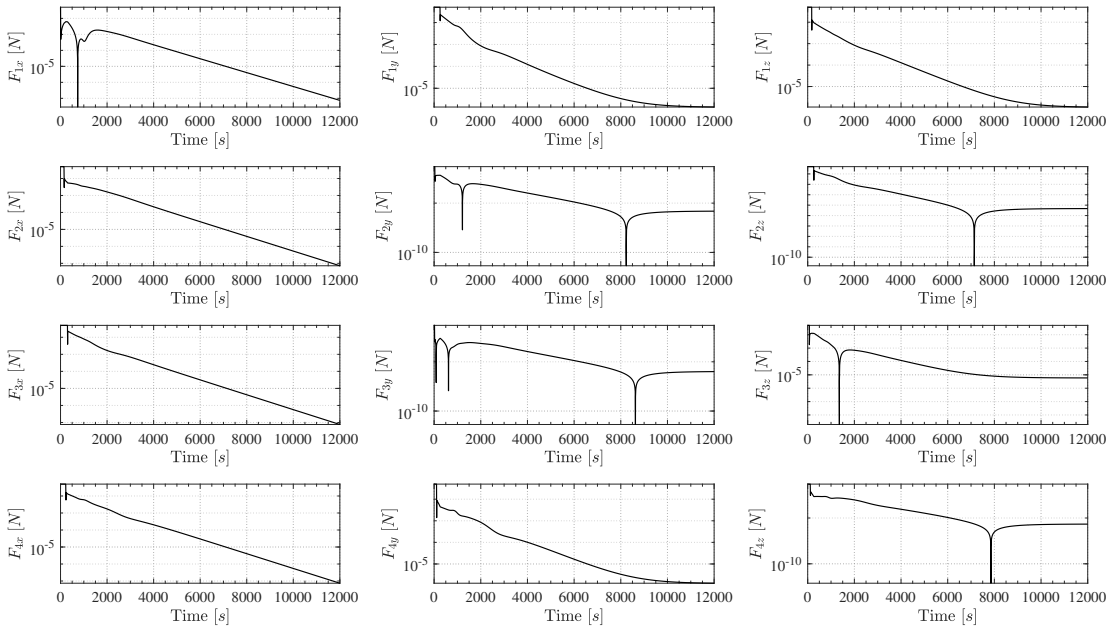

Figure 4.7: *Actuators forces of the spacecrafts over time (no obstacle)*

In Figure 4.7 the actuators forces of the spacecrafts over time are shown. It is noticeable that in the first few instants some of the actuators are using the maximum thrust available. These are the axes where the desired velocities are not equal to the actual velocities.

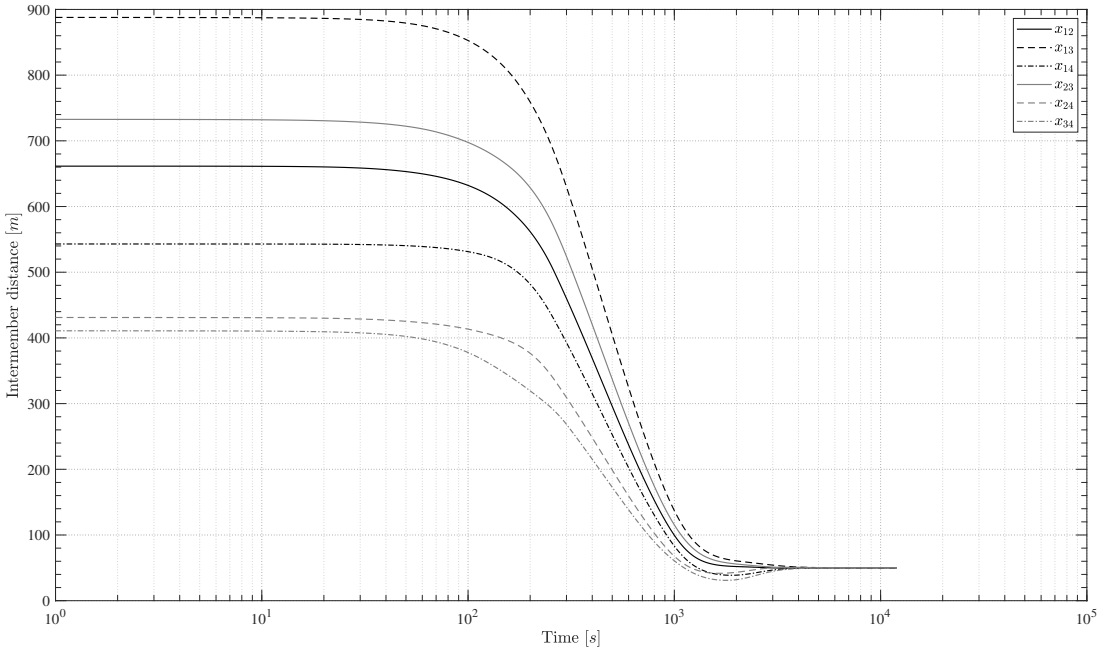

Figure 4.8: *Intermember distance (no obstacle)*

Finally, in Figure 4.8 the intermember distances between the different spacecrafts in the swarm over time are shown. Since the formation is constituted by four spacecrafts, six intermember distances exist. The term x_{ij} in the legend represents the distance between the swarm agent i and the swarm agent j. It appears that each of the intermember distances tends to the final inter spacecraft formation separation value equal to $50\ m$.

4.4 Fixed obstacle simulation

The second scenario contemplates the presence of an obstacle. The objective of the guidance algorithm in this case is to achieve the desired formation in the target position on orbit while avoiding the obstacle. First of all, a simulation without the obstacle was run to predict the trajectories of the spacecrafts if the obstacle wasn't taken into account. After that, the center of the swarm is evaluated over time and the obstacle is placed where the center of the swarm is distant $300\ m$ from the target position. At this point the spacecrafts in the swarm are already close to each other and they are all interacting with the obstacle that will repulse them. The radius of the obstacle is equal to $50\ m$.

In Figure 4.9 the trajectories of the four spacecrafts are represented in the Local-Vertical-Local-Horizontal Frame. The initial positions are illustrated by black circles, the trajectories by a black line, while the red dots represent the final position.

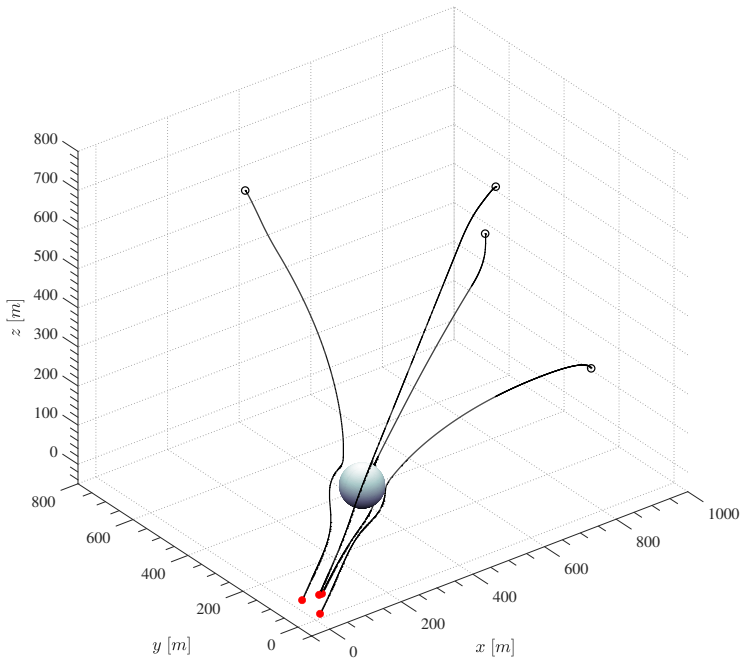

Figure 4.9: *Trajectories of the spacecrafts (fixed obstacle)*

It is noticeable that in this scenario, even if the formation was almost achieved and the spacecrafts in the swarm already close to each other, at a certain point they have to separate each other to avoid the obstacle. Then, they acquire the desired formation in the desired target position as performed in the previous scenario. However, the position of each spacecraft in the formation is not the same as before.

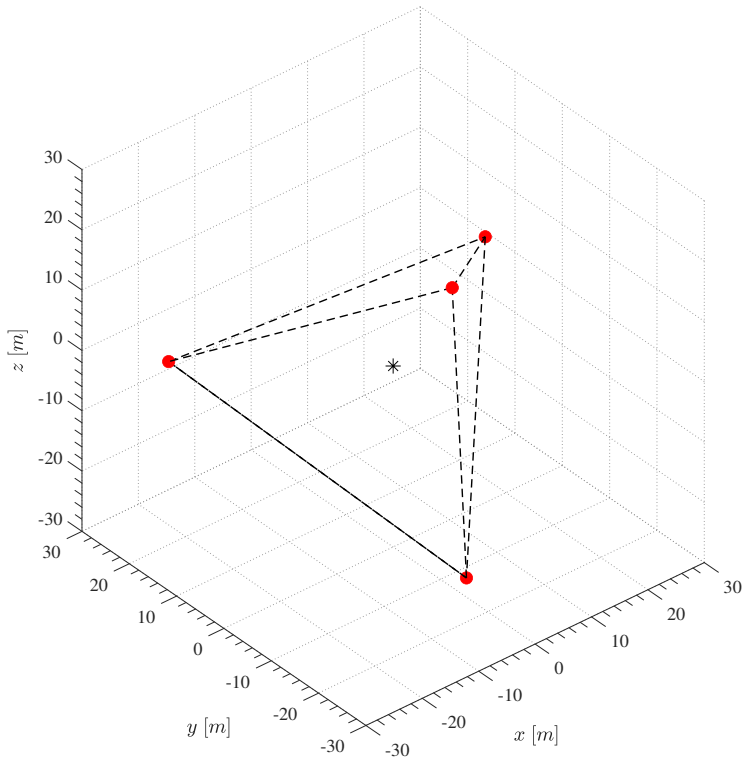

Figure 4.10: *Tetrahedron formation (fixed obstacle)*

In Figure 4.10 a zoom of the tetrahedron formation in shown. As mentioned before, using this approach the final orientation of the tetrahedron in space can't be decided but it depends on the initial condition and on the interaction of the spacecrafts with the external environment. Therefore, since there was an interaction with the obstacle the achieved formation in this scenario is clearly different from the previous one.

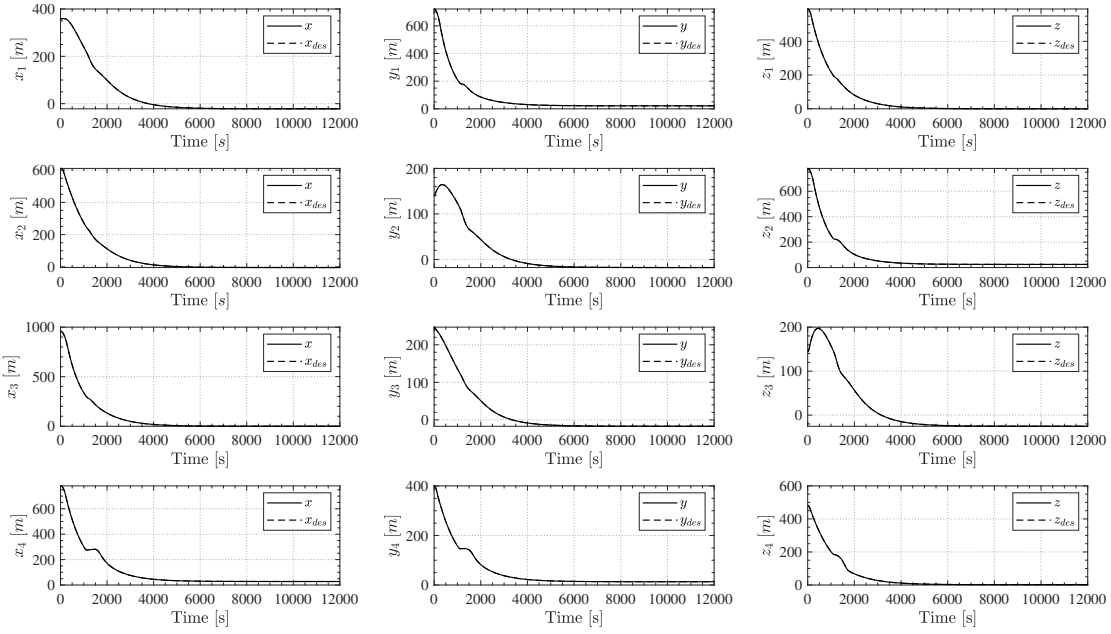

Figure 4.11: *Coordinates of the spacecrafts over time (fixed obstacle)*

In Figure 4.11 the coordinates of the spacecrafts over time are shown. Even on this scenario there is no difference between the desired positions and the actual positions since the continuous line and the dashed line are overlapped.

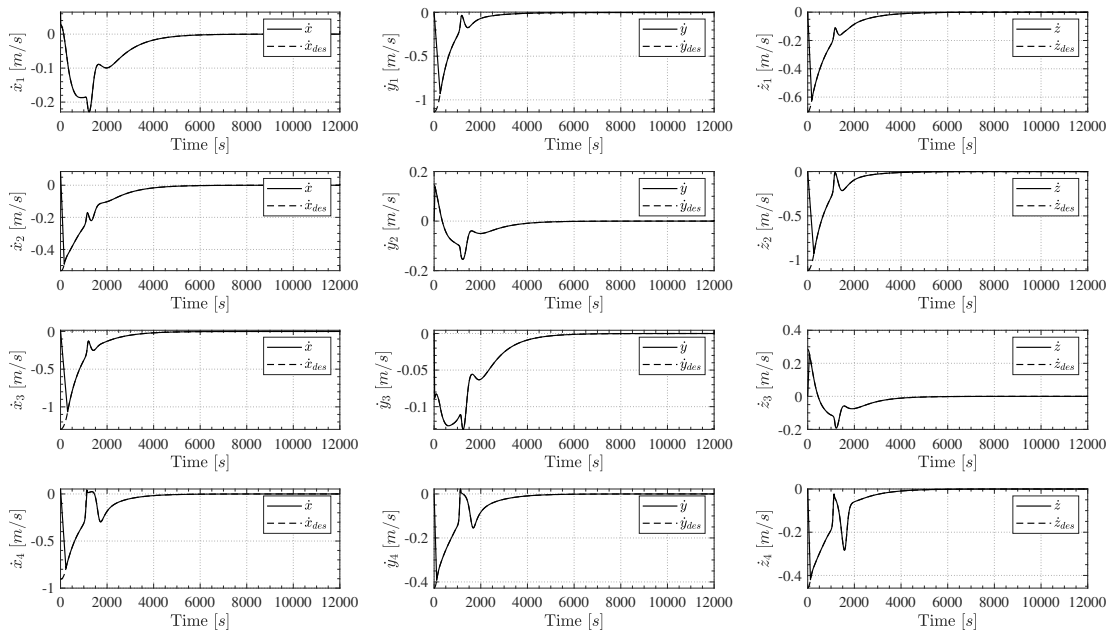

Figure 4.12: *Velocity field of the spacecrafts over time (fixed obstacle)*

In Figure 4.12 the velocity field of the spacecrafts over time is shown. The major changes with respect to the previous scenario are observable within $2000\ s$ from the beginning of the simulation because of the interaction with the obstacle.

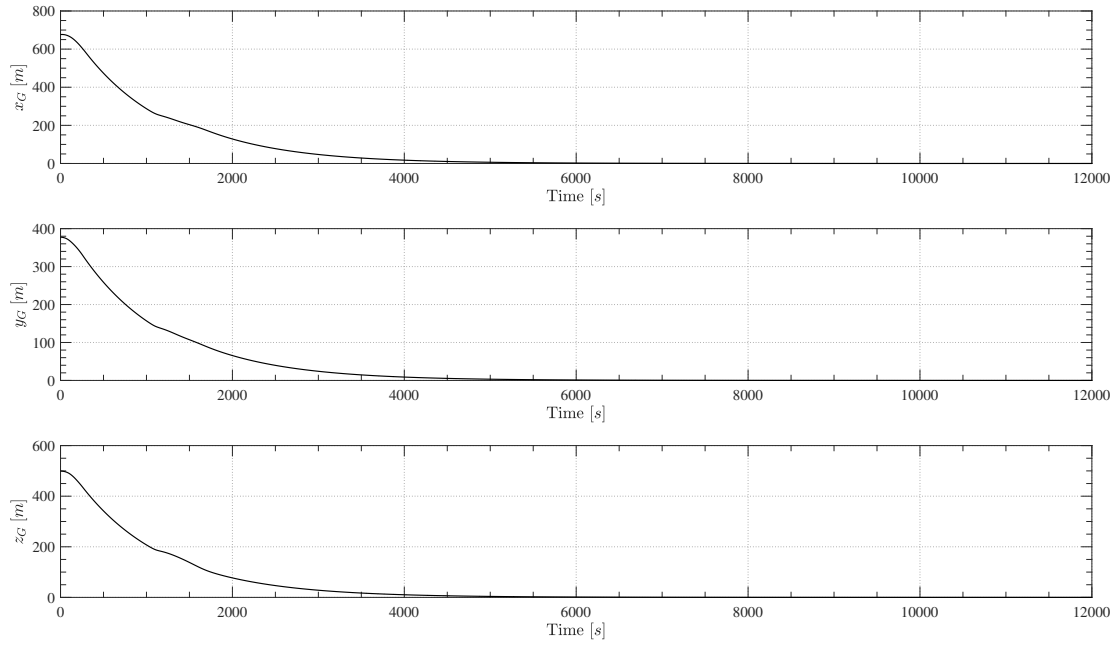

Figure 4.13: *Center of the swarm position over time (fixed obstacle)*

In Figure 4.13 the center of the swarm position over time is shown. It can be seen how all the coordinates decrease to reach the desired target position in the origin of the axes.

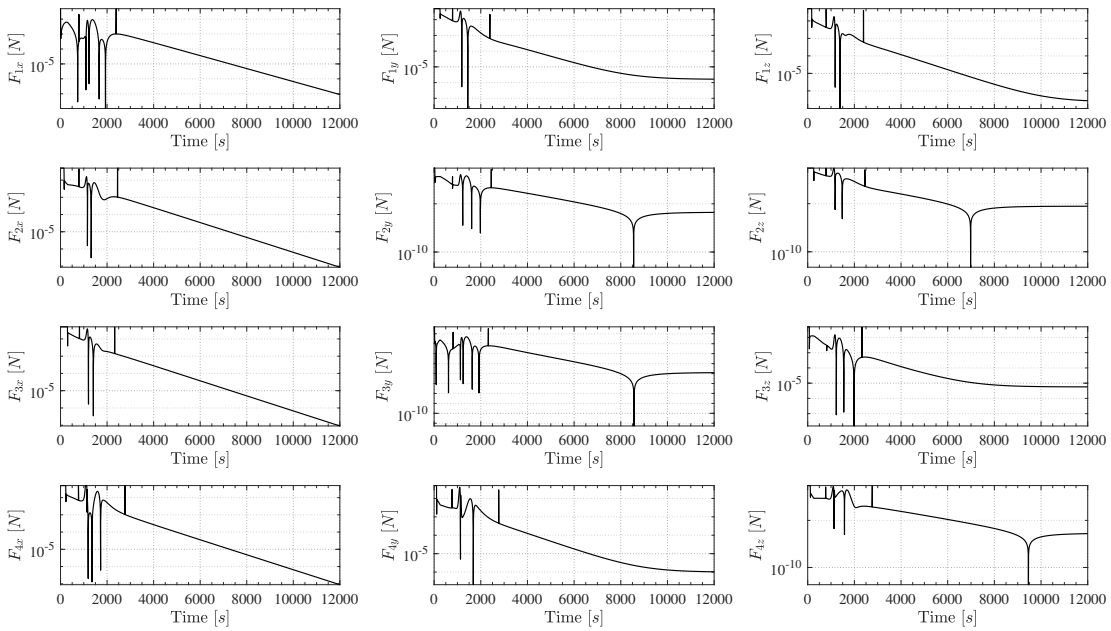

Figure 4.14: *Actuators forces of the spacecrafts over time (fixed obstacle)*

In Figure 4.14 the actuators forces of the spacecrafts over time are shown. It is evident how in this scenario the actuators are used more within the first 2000 s of the simulation because the spacecrafts find themselves to deal with an obstacle that wasn't expected along the way to the target position.

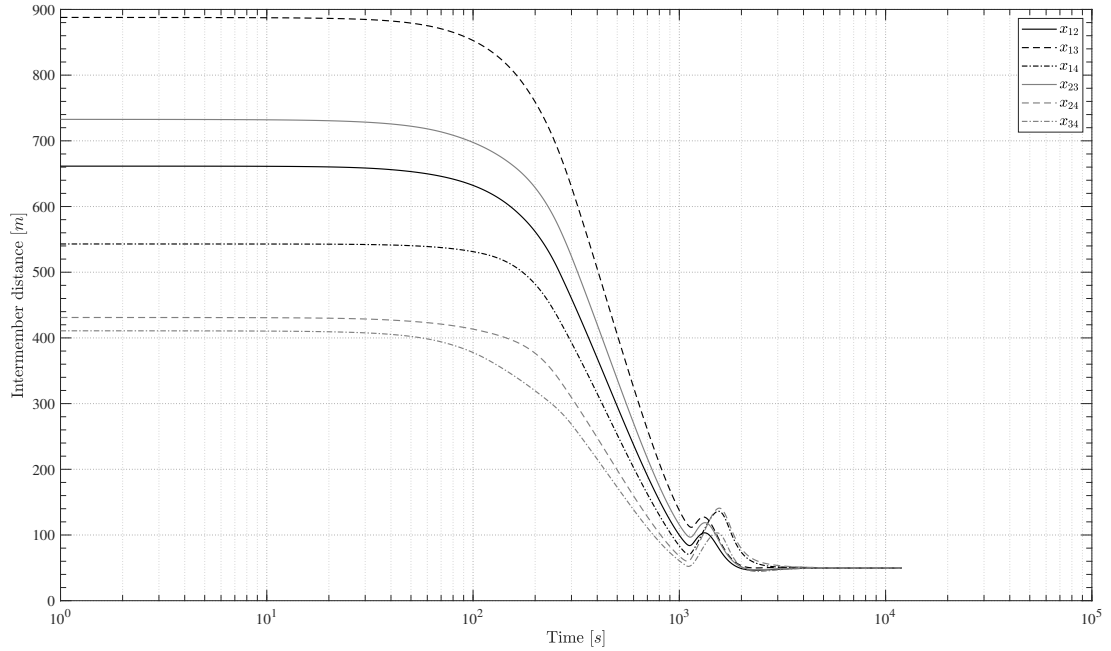

Figure 4.15: *Intermember distance (fixed obstacle)*

In Figure 4.15 the intermember distances between the different spacecrafts in the swarm over time are shown. It can be clearly identified the moment when the spacecrafts interact with the obstacle since the intermember distance among all the spacecrafts increases. After that, the intermember distance tends to $50\ m$ for all of them.

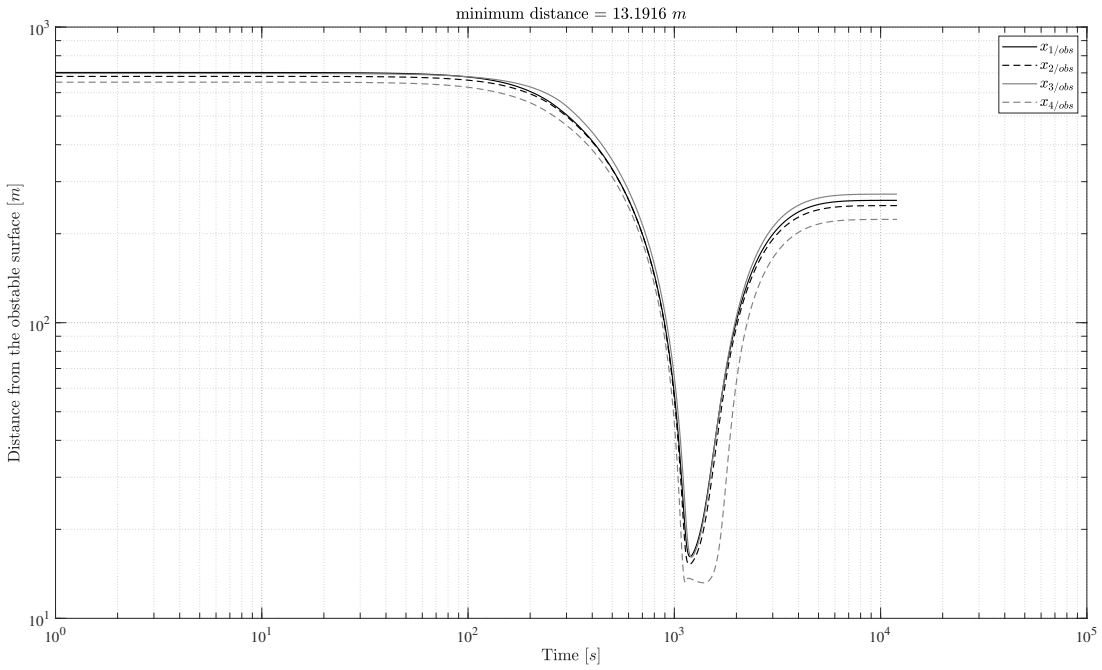

Figure 4.16: *Distance from the obstacle surface (fixed obstacle)*

Lastly, in Figure 4.16 the distance from the obstacle surface for all the spacecrafts in the swarm is shown. It can be seen how the spacecrafts get closer to the obstacle but once they enter the region of influence of the obstacle their trajectories are altered and finally they avoid the obstacle and reach the target location. Since the obstacle is fixed with respect to the origin of the axes, once the formation is achieved the distance from the obstacle is constant over time for all the spacecrafts in the swarm.

4.5 Moving obstacle simulation

The third scenario investigates the presence of a moving obstacle. Once again, a simulation without the obstacle was run to predict the trajectories of the spacecrafts if the obstacle wasn't taken into account.

As for the second scenario, the instant when the center of the swarm is $300\ m$ away from the target position is consider. The aim is to make sure that the center of the obstacle would be in this position simultaneously to the center of the swarm, but now the obstacle has a certain velocity that is not equal to zero. A uniform linear motion is considered for the obstacle, so its position changes over time following the following expression:

$$\bar{x}_{obs} = \bar{x}^0_{obs} + v_{obs}\left(t - t_{obs}\right)\frac{\bar{\alpha}_{obs}}{\left\|\bar{\alpha}_{obs}\right\|} \tag{4.4}$$

where t is the current time, t_{obs} is the time when the center of the swarm is $300\ m$ away from the target position in the first scenario, v_{obs} is a constant parameter representing the magnitude of the velocity of the obstacle, $\bar{\alpha}_{obs}$ is a three-component vector whose components are random real numbers from zero to one. This allows to choose a random direction for the obstacle and consider multiple circumstances in the different simulations.

When $t = t_{obs}$ the second term is equal to zero, as a consequence $\bar{x}_{obs} = \bar{x}^0_{obs}$. This is the same position of the obstacle in the second scenario. The v_{obs} parameter has been chosen of the same order of magnitude of the spacecrafts velocities, thus $0.1\ m/s$.

In Figure 4.17 the trajectories of the four spacecrafts in the Local-Vertical-Local-Horizontal Frame are shown. The initial positions are illustrated by black circles, the trajectories by a black line, while the red dots represent the final position.

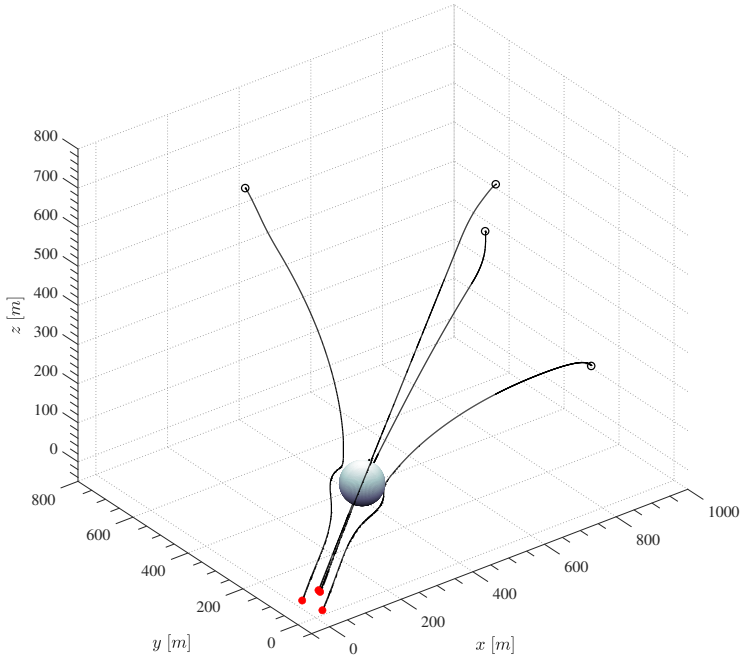

Figure 4.17: *Trajectories of the spacecrafts (moving obstacle)*

In the diagram is shown the obstacle in the moment when $t = t_{obs}$. In this third scenario the trajectories are slightly different because the obstacle is not always in the same position in space but it is moving altering the potential field in which the spacecrafts exist.

In Figure 4.18 the achieved tetrahedron formation is shown. Once again, it is noticeable that the acquired formation is different from the previous ones. In particular, the center of the swarm is always in the origin of the axes but the precise position of each spacecraft in the swarm is different from the previous scenarios.

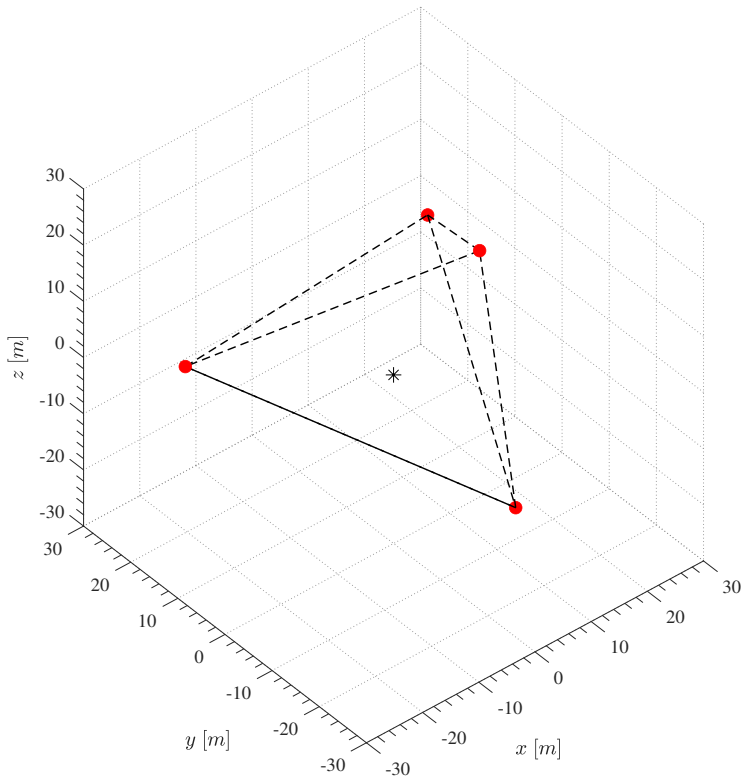

Figure 4.18: *Tetrahedron formation (moving obstacle)*

In Figure 4.19 the coordinates of the spacecrafts over time are shown. The continuous lines, representing the actual positions, and the dashed lines, representing the desired ones, are overlapped, so the controller is guiding the spacecrafts on the desired path. The main difference with the other scenarios is when the spacecrafts interact with the obstacle.

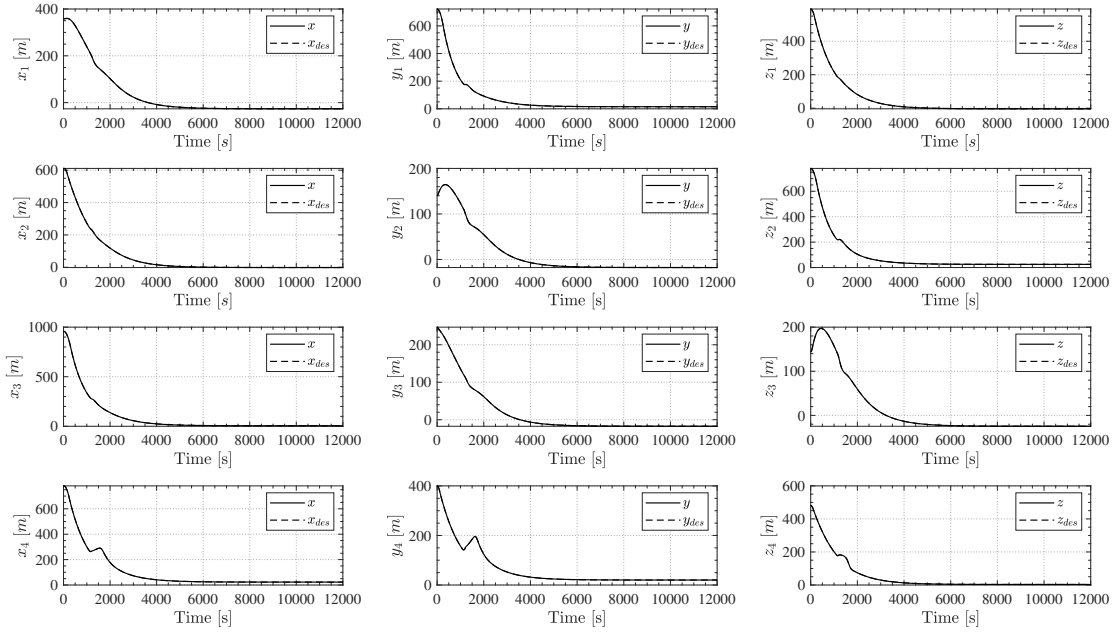

Figure 4.19: *Coordinates of the spacecrafts over time (moving obstacle)*

In Figure 4.20 the velocity field of the spacecrafts over time is shown. As in the previous scenario, at the beginning of the simulation the actual velocities are not equal to the desired ones. However, in this case a non-correspondence between the two velocities can be noticed when the spacecrafts interact with the obstacle. Since the obstacle is moving there is a more drastic change in the potential field.

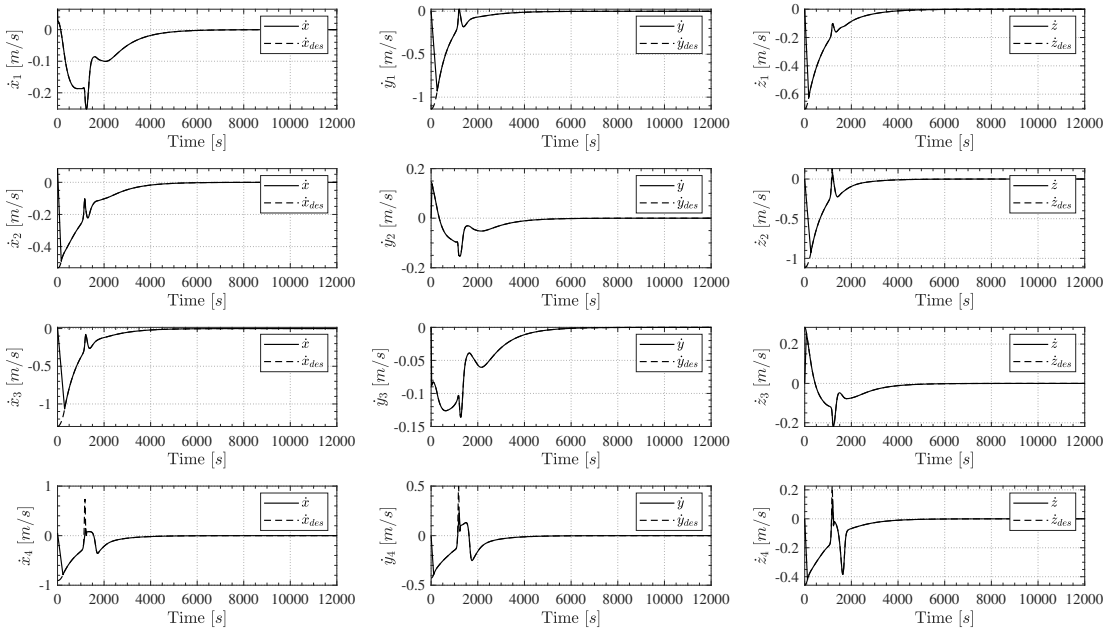

Figure 4.20: *Velocity field of the spacecrafts over time (moving obstacle)*

In Figure 4.21 it can be seen that the center of the swarm reaches the origin of the axes.

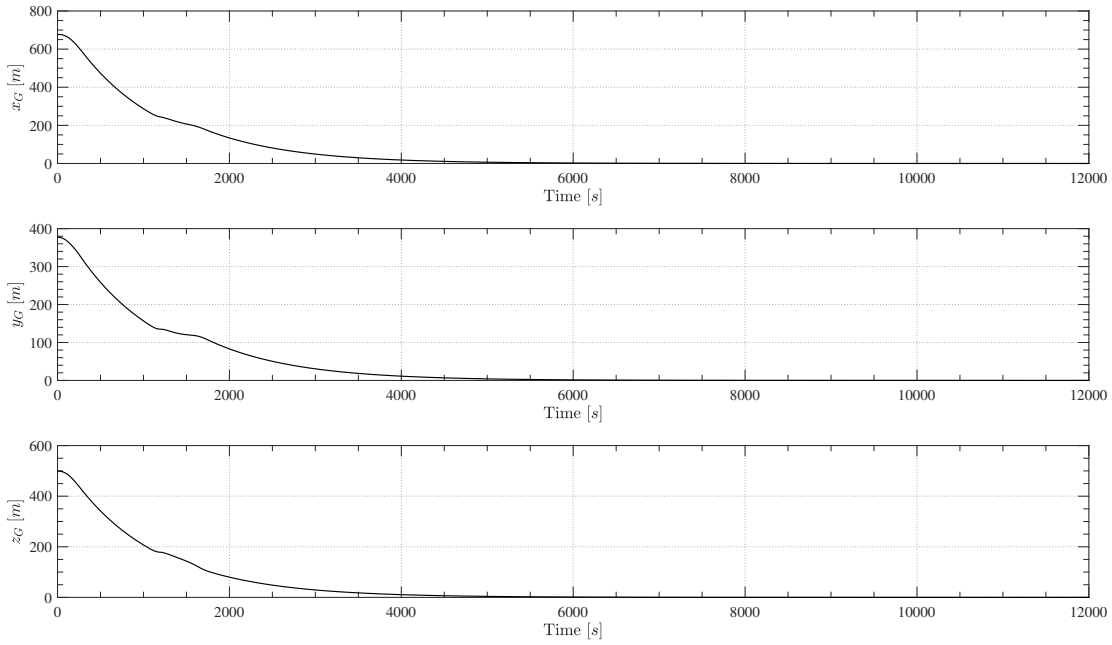

Figure 4.21: *Center of the swarm position over time (moving obstacle)*

In Figure 4.22 the actuators forces of the spacecrafts over time are shown. The highest values of thrust are required at the beginning of the maneuver. In particular, the maximum value available is required at the very beginning and when the spacecrafts reach the region of influence of the obstacle.

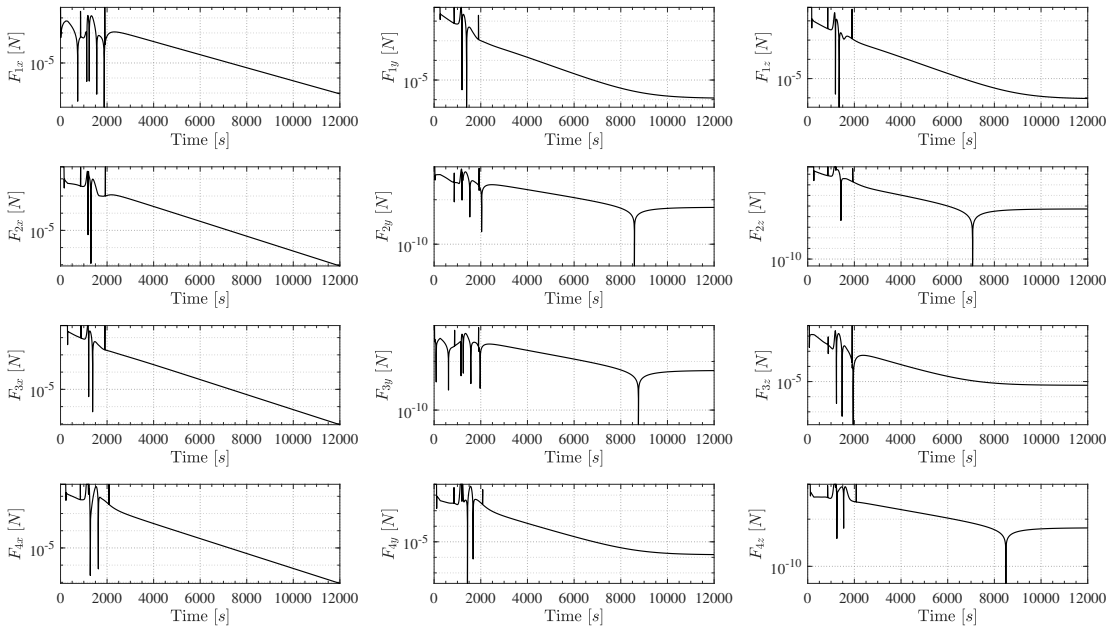

Figure 4.22: *Actuators forces of the spacecrafts over time (moving obstacle)*

In Figure 4.23 the intermember distances between the spacecrafts over time are shown. It can be definitely recognized the moment when the spacecrafts interact with the obstacle.

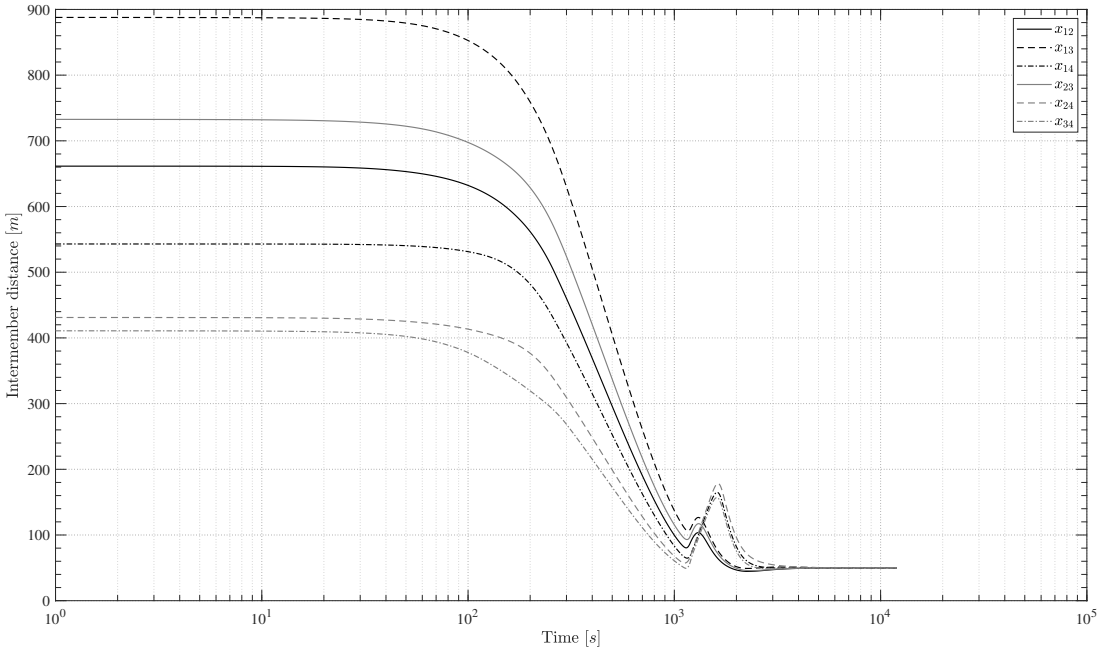

Figure 4.23: *Intermember distance (moving obstacle)*

In this scenario the intermember distances with with one of the spacecrafts are slightly higher in comparison to the third scenario because the obstacle is moving towards the swarm so the spacecrafts have to perform a more drastic maneuver to avoid the obstacle. After that, the intermember distance tends to $50\ m$ for all of them.

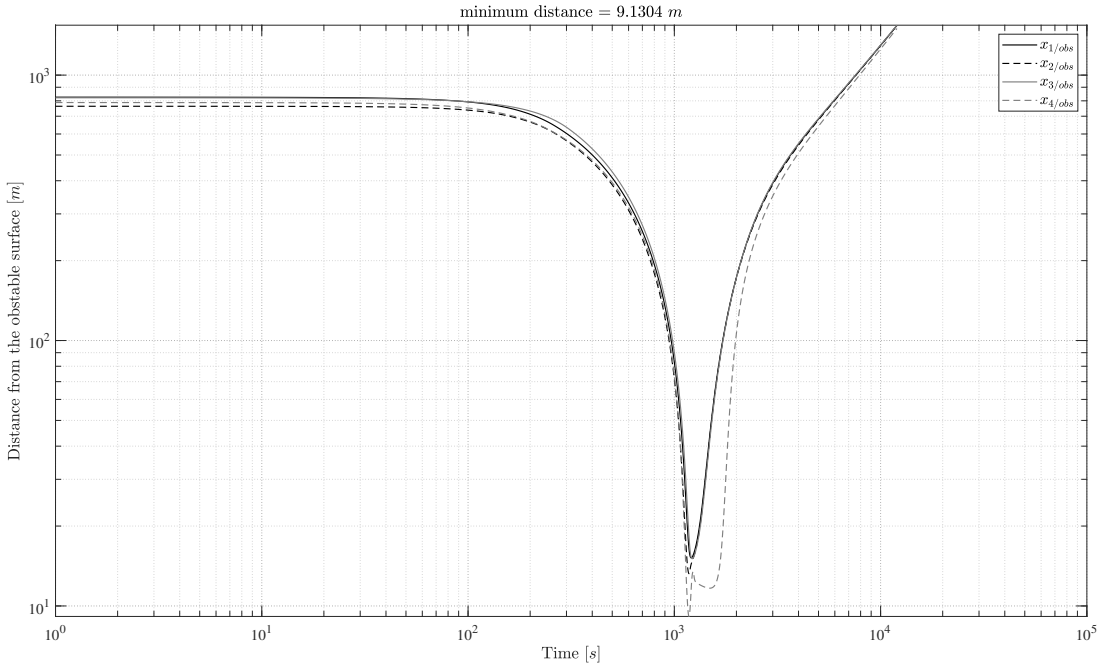

Figure 4.24: *Distance from the obstacle surface (moving obstacle)*

Lastly, in Figure 4.24 the distance from the obstacle surface is shown. It is evident how spacecrafts and obstacle get closer to each other but once the spacecrafts enter the region of influence of the obstacle they are pushed away from it and finally reach the target location. In this scenario the minimum distance from the surface of the obstacle is smaller than the second scenario where the obstacle was fixed in space. In addition, since the obstacle is moving this distance keeps increasing until the end of the simulation.

4.6 Rearranging formation simulation

The fourth scenario tests the capacity of the guidance algorithm to handle a situation where one of the spacecraft in the swarm is no longer operative. The initial condition for this scenario are given by the final configuration of the third scenario, i.e. the one where a moving obstacle was considered. The idea behind the algorithm is that it should check if all the members of the swarm are operative and if one or more are not they can still achieve a different configuration. In the case considered where one spacecraft is inoperative the configuration that they can achieve is an equilateral triangle. Since at the beginning the spacecrafts were arranged in a tetrahedron formation, the remaining three spacecrafts are already forming an equilateral triangle. Therefore, the only thing the algorithm should do is guiding the spacecrafts so that the new center of the swarm is in the origin of the axes.

In Figure 4.25 the trajectories of the remaining three spacecrafts in the Local-Vertical-Local-Horizontal Frame are shown. The center of the swarm is in the origin of the axes.

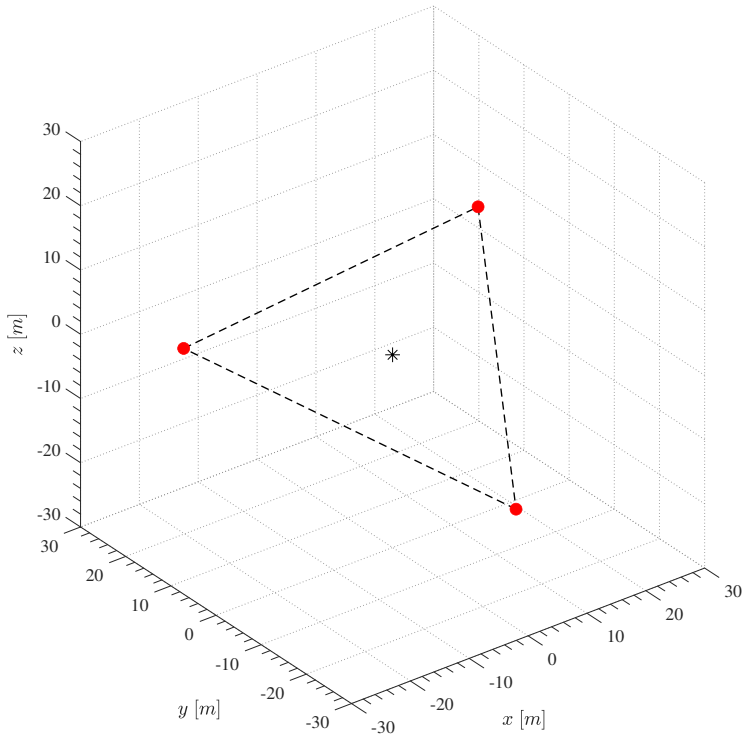

Figure 4.25: *Triangle formation*

In Figure 4.26 the coordinates of the remaining three spacecrafts over time are shown. There is a correspondence between the actual positions and the desired position since the continuous lines and the dashed lines are overlapped. The simulation was run for $8000\ s$ and at the end the center of the swarm reaches the target position.

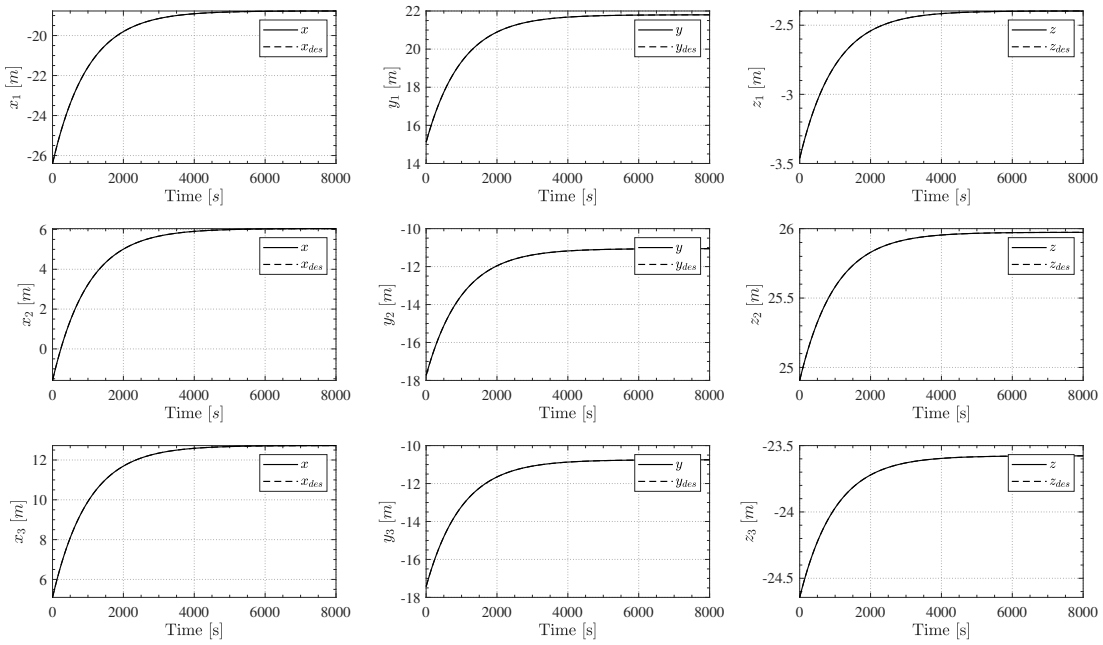

Figure 4.26: *Coordinates of the spacecrafts over time (triangle formation)*

In Figure 4.27 the velocity field of the spacecrafts over time is shown. It can be noticed that the initial velocities are already small because the initial conditions consider a situation where the formation is almost stationary. After that, the velocities keep decreasing since the center of the swarm gets closer to the target position.

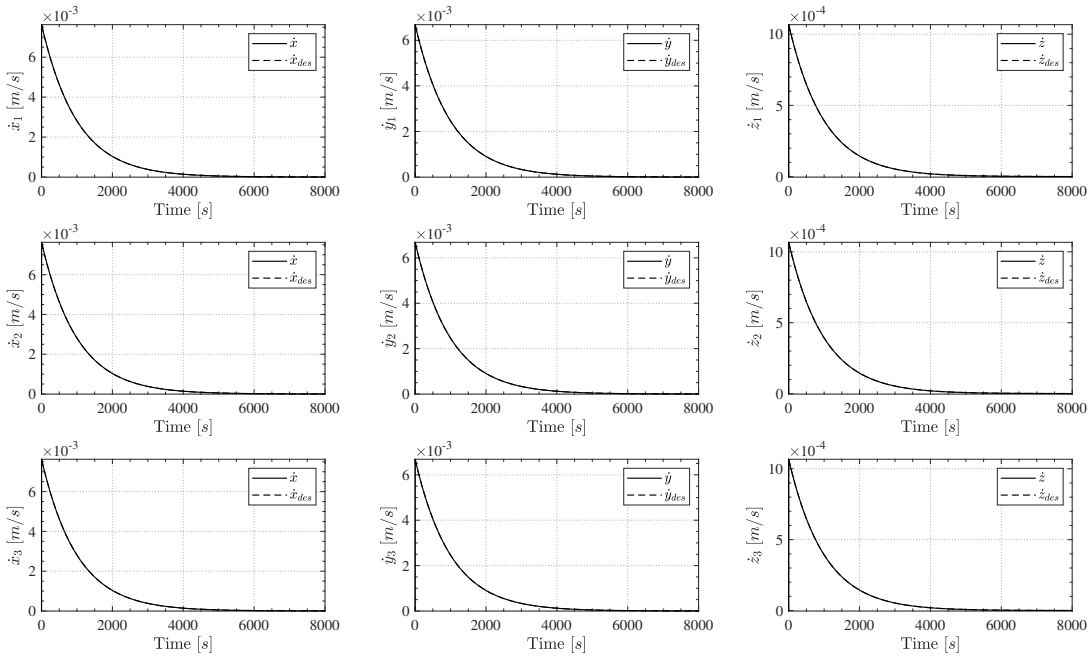

Figure 4.27: *Velocity field of the spacecrafts over time (triangle formation)*

Lastly, in Figure 4.28 the new center of the swarm position over time is shown. Starting from the old position, it moves towards the origin of the axes as expected.

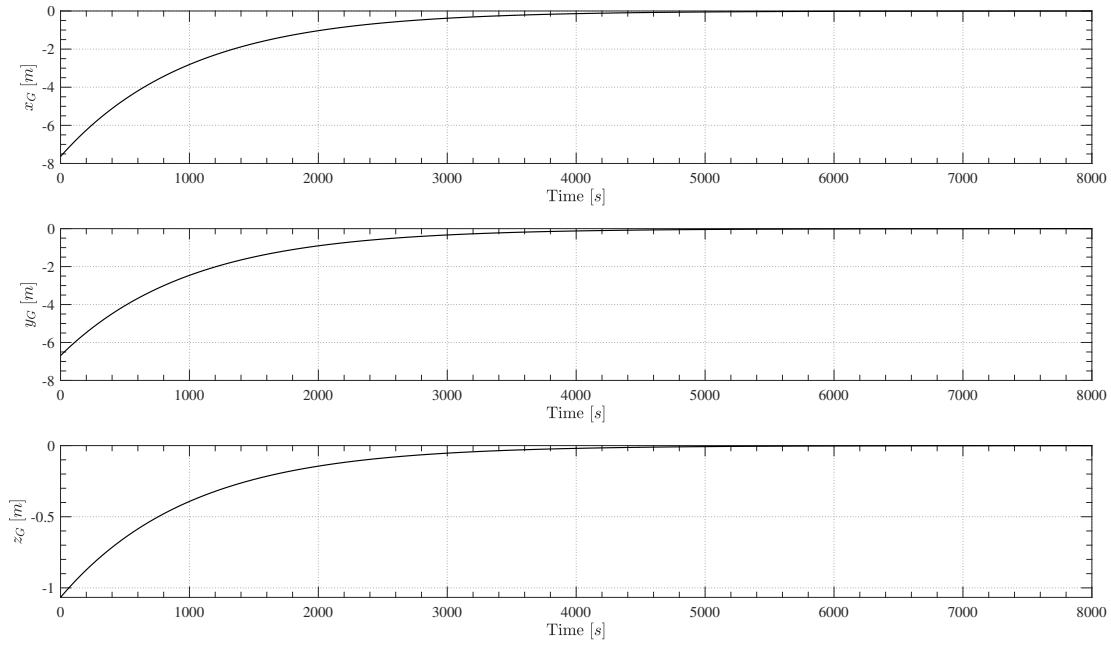

Figure 4.28: *Center of the swarm position over time (triangle formation)*

4.7 Proximity operation simulation

The fifth scenario has the aim to evaluate the maximum dimension of a spherical obstacle that the swarm of spacecrafts can avoid during the formation acquisition maneuver. To do so a proximity operation is considered. In this scenario the initial conditions are different from the previous ones, in fact the magnitude of the distance from each spacecraft to the target position is no longer $1000\ m$ but $50\ m$ instead. The initial positions are evaluated using Equation 4.2 and the initial velocities using Equation 4.3. Moreover, even if the final configuration is always a tetrahedron formation, this time the final inter spacecraft formation separation is reduced to $10\ m$.

As for the previous scenarios a simulation without any obstacles is conducted. This allows to evaluate the trajectories of the four spacecrafts in the swarm that in turn permit to calculate the center of the swarm position over time. The center of the obstacle is placed in the coordinates of the center of the swarm when it is $28\ m$ away from the target position. This value has been chosen to avoid the possibility that one of the spacecrafts is inside the region of influence of the obstacle once the formation is achieved, and at the same time to make this region as big as possible to give more time to the guidance algorithm to perform the collision avoidance maneuver and drive the swarm in the target position.

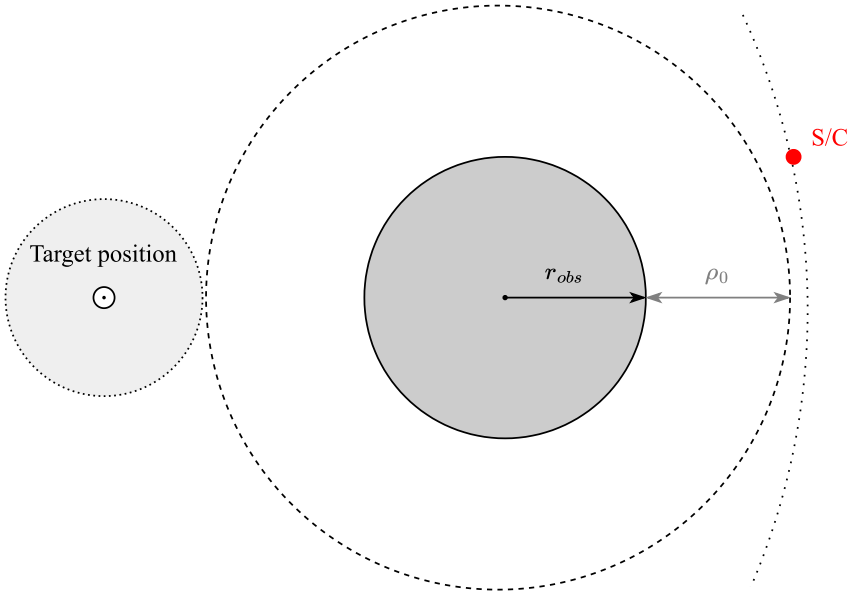

Figure 4.29: *Representation of a possible initial condition*

Different simulations have been run contemplating distinctive initial conditions and for each of them the radius of the obstacle is ranging from $1\ m$ to $10\ m$. The value of the distance of influence of the obstacle is determined by the following expression:

$$\rho_0 = 21 - r_{obs} \tag{4.5}$$

In Figure 4.29 can be seen how the region of influence of the obstacle and the region where the spacecrafts can stay once the formation is achieved do not intersect. The results of the simulations are shown in the following diagrams.

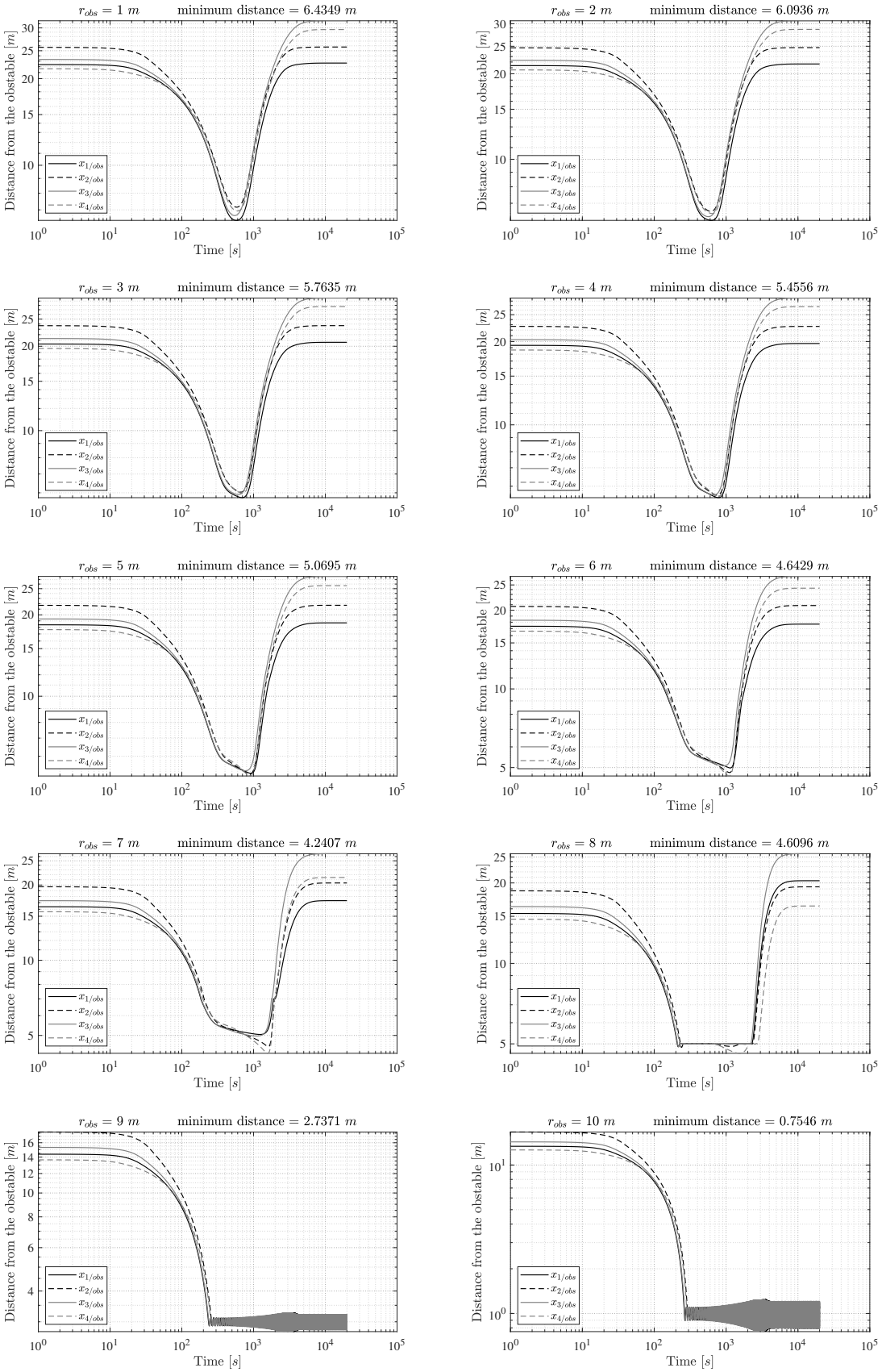

Figure 4.30: *Distance from the obstacle surface (proximity operation)*

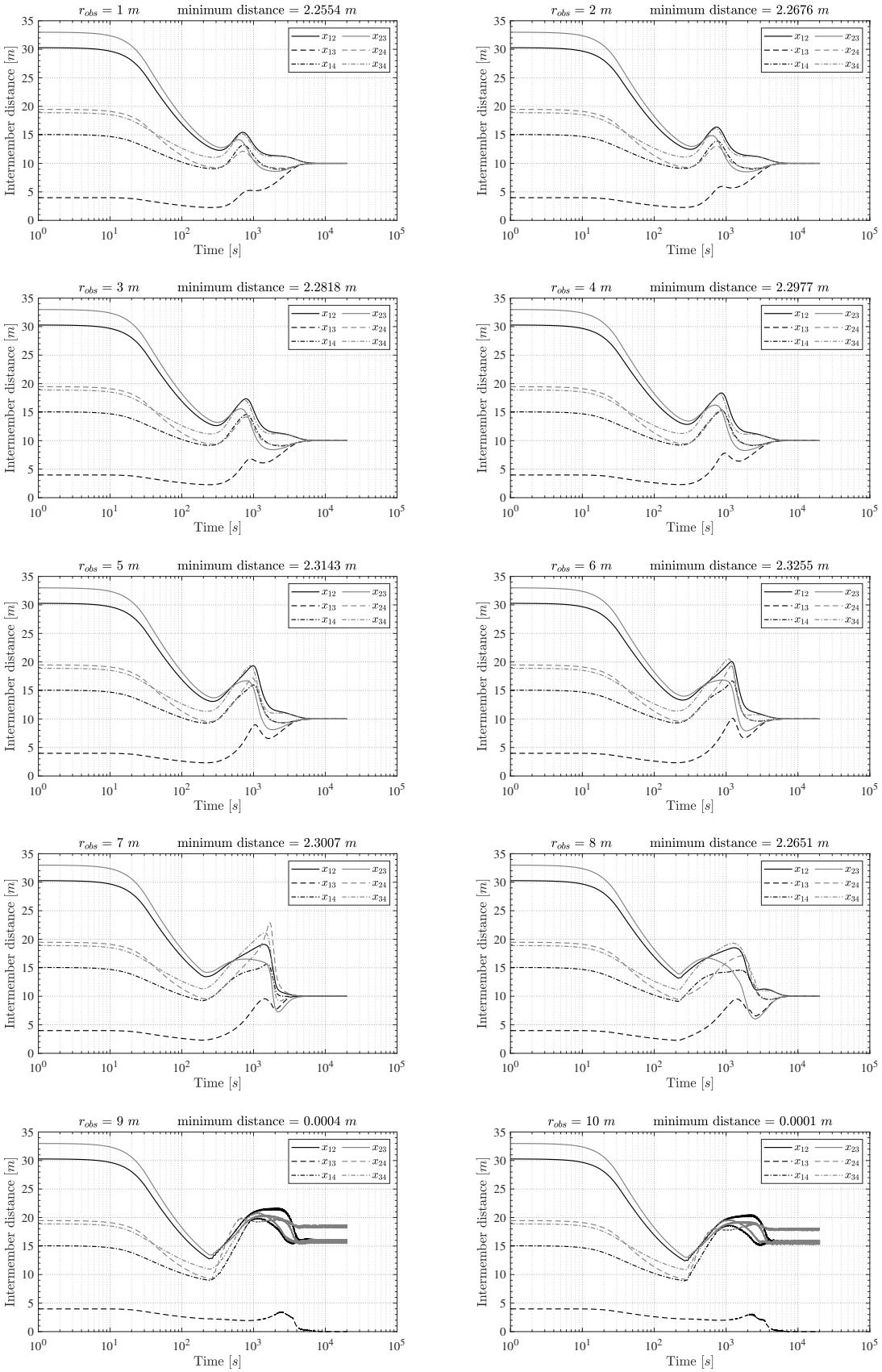

Figure 4.31: *Intermember distance (proximity operation)*

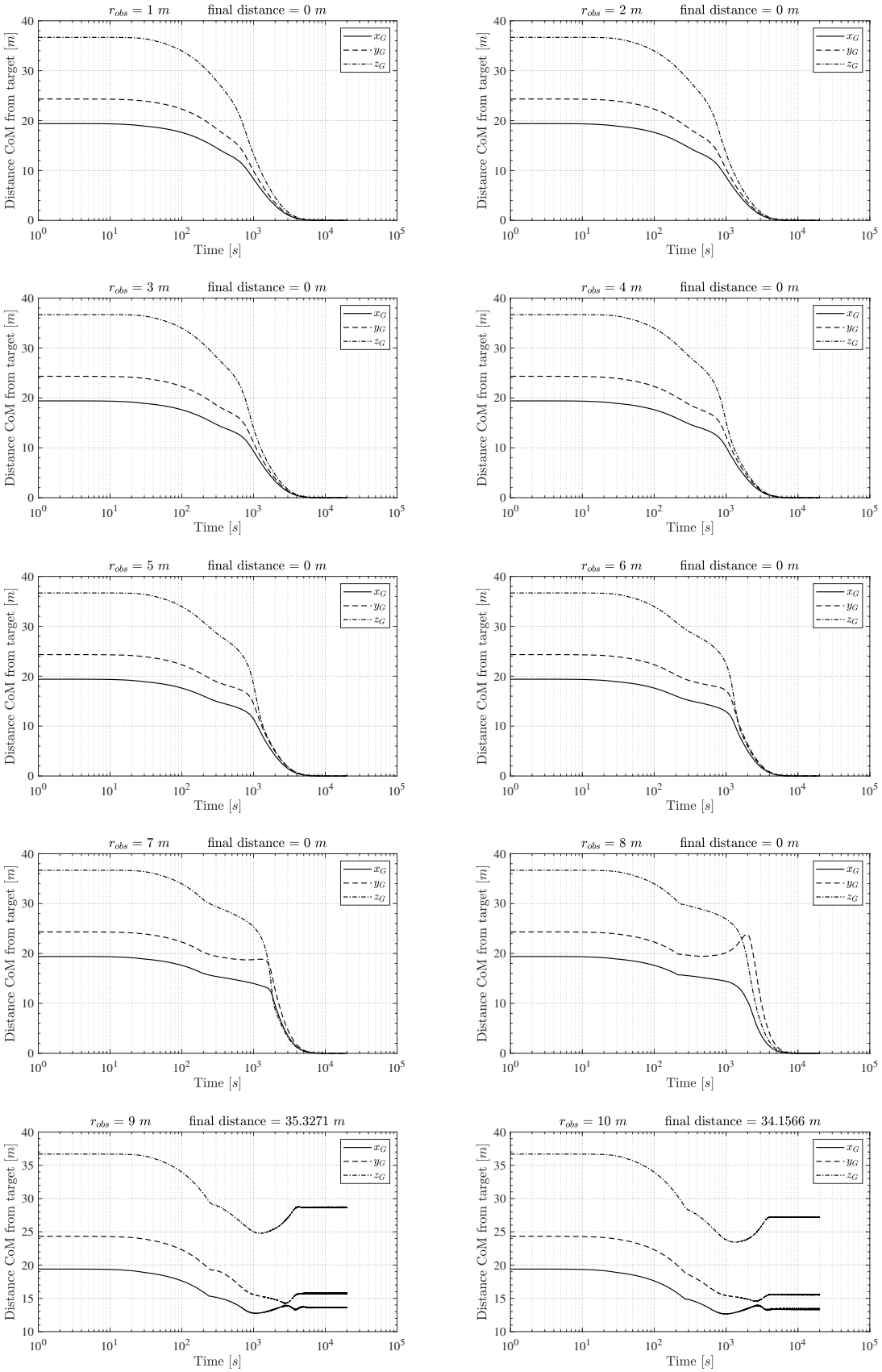

Figure 4.32: *Center of the swarm position over time (proximity operation)*

$\mathbf{r_{obs}}$ $[\mathbf{m}]$	$\lambda_{\mathbf{obs}}^{\mathbf{min}}$ $[\mathbf{m}]$	$\lambda_{\mathbf{int}}^{\mathbf{min}}$ $[\mathbf{m}]$	$\lambda_{\mathbf{cos}}^{\mathbf{fin}}$ $[\mathbf{m}]$
1	6.4349	2.2554	0
2	6.0936	2.2676	0
3	5.7635	2.2818	0
4	5.4556	2.2977	0
5	5.0695	2.3143	0
6	4.6429	2.3255	0
7	4.2407	2.3007	0
8	4.6096	2.2651	0
9	2.7371	0.0004	35.3271
10	0.7546	0.0001	34.1566

Table 4.2: *Proximity operation simulation results*

In Figure 4.30 the distance from the obstacle surface for the ten cases is shown. It can be noticed that for values of the radius of the obstacle less or equal to $8\ m$ the spacecrafts get closer to the obstacle and then avoid it because then this distance increase again. Conversely, in the last two cases at some point this distance oscillates around a certain value but do not increase anymore. This is a symptom that something is not working the way it should even if there is not a collision with the obstacle.

In Figure 4.31 the intermember distance for the ten cases is shown. Once again, considering the first eight cases the intermember distance tends to $10\ m$ for all the spacecrafts in the swarm, but in the last two cases they are all different. In particular, the minimum distance between the swarm agent 1 and the swarm agent 3 goes to zero because the two spacecrafts collide with each other. This is caused by the fact that there is a region with a local minimum created by the combination of the attractive potential and the repulsive potential in which the spacecrafts sink.

In Figure 4.32 the center of the swarm position over time for the ten cases is shown. Each diagram represents the three coordinates in the Local-Vertical-Local-Horizontal Frame and they are expected to go to zero since the target position corresponds to the origin of the axes. As foreseen, this is the case for the first eight cases, but not for the last two cases since the formation is not achieved.

In Table 4.2 the main results from the proximity operation simulation are presented. In particular, for the different values of the radius of the obstacle the values of the minimum distance from the obstacle (λ_{obs}^{min}), the minimum intermember distance (λ_{int}^{min}) and the final distance of the center of the swarm (λ_{cos}^{fin}) are summarized. It is clear that in the last two cases the algorithm is not able to guide the spacecrafts in the target position and achieve the desired formation avoiding the obstacle.

Chapter 5

Conclusions

Distributed space systems are expected to be the new tendency for space missions. This kind of mission will require GNC algorithms that are more flexible and less computationally demanding than the ones already available in literature. This thesis work answers this need by proposing a GNC algorithm architecture for formation flying spacecraft reconfiguration. The guidance algorithm is based on the APF method, which implements an active collision avoidance based on a repulsive field.

The GNC algorithm has been validated through numerical simulations after building a model in a Matlab-Simulink environment. Different scenarios have been analyzed to test the performance of the algorithm. The first scenario is designed to demonstrate the effectiveness of the algorithm to guide the spacecrafts in the swarm from a random initial configuration to the desired one whose center is located at a specific position in orbit while avoiding the collision only with other members of the swarm. The second scenario contemplates the presence of a fixed obstacle, while the third scenario a moving obstacle, in both cases the spacecrafts should reach the desired configuration while avoiding the obstacle. The fourth scenario analyzes the ability of the swarm to rearrange the formation based on the number of spacecrafts, in particular, the reconfiguration from the tetrahedron formation to the equilateral triangle formation has been considered. The last scenario evaluates the maximum dimension of a spherical obstacle that the swarm of spacecrafts is able to avoid in a proximity operation situation during the maneuver.

In some simulations regarding the proximity operation scenario the agents could not reach the final desired formation and got stuck in an undesired equilibrium position. From the Equilibrium Shaping it is known that the final relative geometry is an equilibrium point for the system but the global stability is not guaranteed. In fact, depending on the choice of the potential function, other equilibrium points may exist and be stable as well, driving the swarm towards an undesired configuration. This problem is commonly referred to as local minima problem and there are several ways it can be dealt with. A very effective approach consists in activating a procedure when the spacecraft evaluates its desired velocity to be zero [25]. Then, the agent should check if its current position allows the desired final configuration to be achieved. If this is not the case, a possibility would be to change the value of the constant parameters in the potential function just for the interested agent. Consequently, the presence of these local minima increase the fuel consumption for the spacecrafts that get stuck in one of them. Future work to improve the reliability of the algorithm should focus on the implementation of this procedure.

Bibliography

[1] Chakravarthini M Saaj, Vaios Lappas, and Veysel Gazi. Spacecraft swarm navigation and control using artificial potential field and sliding mode control. In *2006 IEEE International Conference on Industrial Technology*, pages 2646–2651. IEEE, 2006.

[2] Kyle T Alfriend, Srinivas R Vadali, Pini Gurfil, Jonathan P How, and Louis Breger. *Spacecraft formation flying: Dynamics, control and navigation*, volume 2. Elsevier, 2009.

[3] Hanspeter Schaub. Spacecraft formation flying. `https://hanspeterschaub.info/research-ff.html`.

[4] National Aeronautics and Space Administration. Formation flying. `https://www.nasa.gov/centers/ames/engineering/divisions/spaceflight/flight-dynamics/formation-flying`.

[5] European Space Agency. Formation flying. `https://sci.esa.int/web/sci-ft/-/37936-formation-flying`.

[6] Steve Chien, Rob Sherwood, Gregg Rabideau, Rebecca Castano, Ashley Davies, Michael Burl, Russell Knight, Tim Stough, Joe Roden, Paul Zetocha, et al. The techsat-21 autonomous space science agent. In *Proceedings of the first international joint conference on Autonomous agents and multiagent systems: part 2*, pages 570–577, 2002.

[7] European Space Agency. esa - cluster overview. `https://www.esa.int/Science_Exploration/Space_Science/Cluster_overview2`.

[8] C. P. Escoubet, M. Fehringer, and M. Goldstein. Introductionthe cluster mission. *Annales Geophysicae*, 19(10/12):1197–1200, 2001.

[9] European Space Agency. esa - grace mission. `https://earth.esa.int/eogateway/missions/grace`.

[10] OHB Sweden. ohb - prisma mission. `https://www.ohb-sweden.se/space-missions/prisma`.

[11] European Space Agency. esa - proba mission. `https://www.esa.int/Enabling_Support/Space_Engineering_Technology/Proba_Missions/Proba-3_mission2a`.

[12] European Space Agency. esa - proba mission. https://www.esa.int/Enabling_Support/Space_Engineering_Technology/Proba_Missions/Proba-3_Mission3.

[13] European Space Agency. Lisa - eoportal. https://www.eoportal.org/satellite-missions/lisa-observatory.

[14] National Aeronautics and Space Administration. Lisa. https://lisa.nasa.gov/.

[15] Joseph N Pelton and Scott Madry. *Handbook of Small Satellites: Technology, Design, Manufacture, Applications, Economics and Regulation*. Springer, 2020.

[16] European Space Agency. esa - swarm mission. https://earth.esa.int/eogateway/missions/swarm.

[17] Farah Alibay, Justin C Kasper, T Joseph W Lazio, and Tim Neilsen. Sun radio interferometer space experiment (sunrise): tracking particle acceleration and transport in the inner heliosphere. In *2017 IEEE Aerospace Conference*, pages 1–15. IEEE, 2017.

[18] Jet Propulsion Laboratory NASA. nasa - sunrise mission. https://www.jpl.nasa.gov/missions/sun-radio-interferometer-space-experiment.

[19] Stefano Silvestrini, Vincenzo Pesce, Michele Lavagna, et al. Distributed autonomous guidance, navigation and control loop for formation flying spacecraft reconfiguration. In *5th CEAS Specialist Conference on Guidance, Navigation and Control-EuroGNC*, pages 1–19, 2019.

[20] Wigbert Fehse. *Automated rendezvous and docking of spacecraft*, volume 16. Cambridge university press, 2003.

[21] Roger R Bate, Donald D Mueller, Jerry E White, and William W Saylor. *Fundamentals of astrodynamics*. Courier Dover Publications, 2020.

[22] Howard Curtis. *Orbital mechanics for engineering students*. Butterworth-Heinemann, 2013.

[23] David A Vallado. *Fundamentals of astrodynamics and applications*, volume 12. Springer Science & Business Media, 2001.

[24] United States Committee on Extension to the Standard Atmosphere, United States. Air Force, United States. Weather Bureau, United States. National Oceanic, and Atmospheric Administration. *US standard atmosphere*. National Oceanic and Amospheric [sic] Administration, National Aeronautics ..., 1962.

[25] Dario Izzo and Lorenzo Pettazzi. Equilibrium shaping: distributed motion planning for satellite swarm. In *Proc. 8th Intern. Symp. on Artificial Intelligence, Robotics and Automation in space*, volume 25, 2005.

[26] Lorenzo Pettazzi, Dario Izzo, and S Theil. Swarm navigation and reconfiguration using electrostatic forces. In *7th International Conference on Dynamics and Control of Systems and Structures in Space, Greenwich, London, England*, pages 257–267. Citeseer, 2006.

[27] Lorenzo Pettazzi, Hans Krüger, Stephan Theil, and Dario Izzo. Electrostatic forces for satellite swarm navigation and reconfiguration. *esa report*, 2006.

[28] Veysel Gazi. Swarm aggregations using artificial potentials and sliding-mode control. *IEEE Transactions on Robotics*, 21(6):1208–1214, 2005.

[29] Nicoletta Bloise, Elisa Capello, Hyeongjun Park, Elisabetta Punta, and Marcello Romano. Artificial potential field and sliding mode strategies for proximity operations with obstacle avoidance. In *2018 15th International Workshop on Variable Structure Systems (VSS)*, pages 221–226. IEEE, 2018.

[30] Mauro Mancini, Nicoletta Bloise, Elisa Capello, and Elisabetta Punta. Sliding mode control techniques and artificial potential field for dynamic collision avoidance in rendezvous maneuvers. *IEEE Control Systems Letters*, 4(2):313–318, 2019.

[31] Nicoletta Bloise, Elisa Capello, Matteo Dentis, and Elisabetta Punta. Obstacle avoidance with potential field applied to a rendezvous maneuver. *Applied Sciences*, 7(10):1042, 2017.

[32] Graham Clifford Goodwin, Stefan F Graebe, Mario E Salgado, et al. *Control system design*, volume 240. Prentice Hall Upper Saddle River, 2001.

[33] Liuping Wang. *PID control system design and automatic tuning using MATLAB/Simulink*. John Wiley & Sons, 2020.